Comput Geosci (2017) 21:1289–1312
DOI 10.1007/s10596-017-9692-6

ORIGINAL PAPER

A model for non-Newtonian flow in porous media at different flow regimes

Arild Lohne[1,2] · Oddbjørn Nødland[1,2,3] · Arne Stavland[1,2] · Aksel Hiorth[1,2,3]

Received: 30 September 2016 / Accepted: 8 August 2017 / Published online: 18 August 2017

Abstract Polymeric liquids are of great practical importance for porous media flow as they can be used to improve the sweep of water in the reservoir and therefore improve the recovery of oil. Due to the non-Newtonian behavior of these liquids, they are extremely challenging to model. In this paper, we present a model that is capable of describing the most commonly observed flow regimes in porous media: (i) Newtonian, (ii) Shear thinning, (iii) Shear thickening, and (iv) Mechanical degradation. The novel feature of our model is that the time constants for the shear thinning and shear thickening behavior are related to variations in reservoir properties and conditions, thus making it possible to translate lab results to larger scale without introducing new fitting parameters. Furthermore, we present a way to estimate polymer mechanical degradation in porous media. In our model, the polymer degradation rate is linked to the effective pore radius (using a Kozeny-Carman type equation), shear stress, and polymer molecular weight, M_w. The degradation results in a lower M_w, while the polymer volumetric concentration is unaffected. The model is applied to a series of laboratory core flood experiments conducted with partially hydrolyzed polyacrylamide, HPAM, of different initial M_w ranging from 5 to 20 MDa in seawater, and core permeability varied from 137 to 2019 mD. The flow rate is varied approximately three orders of magnitude and covers the shear thinning, shear thickening, and degradation flow regimes. We show that our model is able to reproduce experimental rate-dependent flow resistance, as well as viscosity of effluent samples. An important aspect supporting the use of the model as a predictive tool is that all the simulations with a given brine have made use of a single set of input parameters to describe the observed shear thickening and degradation behavior. Simulation of a second experimental series using low salinity brine required a separate set of input parameters for the shear thickening and shear degradation. The onset of shear thickening was not affected while shear thickening was reduced and degradation appeared to be slower.

Keywords Polymer flooding · Reservoir simulation · EOR · Shear thickening · Polymer degradation · Porous media

1 Introduction

Polymers added to the injection brine increase the aqueous phase viscosity and can decrease the water permeability. This can result in better sweep and hence, in faster production of oil [60]. However, many factors must be considered for a proper evaluation of a polymer flooding project. Aside from important practical issues, such as economic viability and environmental concerns, there are still many theoretical challenges related to predicting the behavior of polymeric liquids inside the reservoir. In particular, we need to improve our understanding of the different rheological flow regimes of the polymer, and how they depend upon local variations in the reservoir parameters, such as porosity, permeability, temperature, and brine salinity. This is crucial to obtain predictive accuracy for polymer flooding at the field scale.

✉ Oddbjørn Nødland
oddbjorn.m.nodland@uis.no

1 The National IOR Centre of Norway, Stavanger, Norway

2 International Research Institute of Stavanger (IRIS), Stavanger, Norway

3 University of Stavanger, Stavanger, Norway

The main difficulty in modelling polymer flooding lies in the fact that EOR polymers are non-Newtonian fluids. For Newtonian fluids, there is a linear relationship between the shear stress and the rate of strain, $\tau = \eta\dot{\gamma}$, where the slope is the viscosity of the fluid. For non-Newtonian fluids, the dynamical behavior is encoded in the stress tensor, which is determined from constitutive equations [2]. Given a set of such equations, a relationship between flow rate and pressure drop can be found. For porous media flow, this is very challenging as the pore geometry is non-uniform and the shear rate vary from point to point in space. Nevertheless, to describe polymeric flow in porous media it is common to define an apparent shear rate, which is proportional to the Darcy velocity, u, and inversely proportional to the square root of the porosity and permeability, $\dot{\gamma} \propto u/\sqrt{k\phi}$. The apparent viscosity is defined from Darcy's law, $\eta = -k\nabla p/u$. For very low apparent shear rates, the apparent viscosity may be approximately constant (Newtonian flow regime), but at increasing levels of shear it tends to become shear thinning. This is especially the case for biopolymers such as xanthan, which have been consistently observed to display shear thinning behavior in bulk solutions, as well as when flowing through porous rock samples. On the other hand, for synthetic polymers such as HPAM, additional effects are usually observed in porous media as the shear rate increases. For these polymers, experiments have repeatedly revealed pronounced dilatant effects at higher shear rates ("apparent shear thickening"), resulting in a dramatic increase in the macroscopic flow resistance [9, 11, 23, 34]. In coreflooding experiments performed at flow rates in this regime, the additional pressure drop can be several orders of magnitude larger than the corresponding pressure drop for a purely shear thinning polymer.

Another critical factor to consider is polymer mechanical degradation in porous media. It is well documented that when sufficient extensional forces are applied, covalent bonds along the polymer chain backbone may rupture [39, 51]. When this happens, the polymer is split up into smaller molecules, and depending on the number of chain scission events, it can lead to a dramatic, permanent decrease in the effective viscosity of the polymer solution. Obviously, the issue of mechanical degradation is especially critical in and around the injection/production facilities, where the molecules are exposed to high shear rates and, possibly, to turbulent flow [67]. Moreover, it has been recognized that the amount of degradation will be a function of the reservoir heterogeneity in the near well region (e.g., [61, 64]). Thus, if proper care is not taken as to minimize the degradation, the EOR potential on the field will be greatly compromised [55]. In one recent field case, polymer degradation was observed to give a 75% reduction in the low shear viscosity, whereas beforehand it had only been expected to be 25% [41].

In order to better quantify the uncertainties surrounding a polymer flooding project, it is therefore important to include all of the relevant physics into the simulation tools used to forecast the performance of the polymer flood. A challenge with models for polymers in a porous medium is that they tend to contain a large number of parameters that needs to be manually tuned for each particular application. However, in a field case there will, in addition to spatial variation in permeability and porosity, be (possibly large) gradients in temperature and salinity, stemming from differences between the injection and formation brines. Temperatures deep within the reservoir are typically much higher than the injected water, and the ion concentrations that are injected are usually lower than those already present in the formation. Variations in all of these parameters will alter the fluid rheology, and this needs to be captured in simulation models. Furthermore, in situations where the elastic contributions to the flow resistance become important, it is necessary to have a suitable model for polymer mechanical degradation, as this process will start to have an impact shortly after the onset of the shear thickening flow regime.

The purpose of this paper is two-fold: (i) to present a new, "unified" simulation model for polymer flooding and, in particular, (ii) to present a model for polymer mechanical degradation in porous media. The model covers all the experimentally observed flow regimes in porous media, and it is compared, successfully, with experimental results over a wide range of flow rates and permeabilities. With our approach, the time constants that define the transition between the various flow regimes are related to reservoir parameters, such as permeability, porosity, temperature etc. As a result, we are able to greatly reduce the amount of free parameters, thus allowing for an easier upscaling of lab results. We demonstrate that we can simulate the behavior of different polymers with mostly the same set of input parameters.

The rest of this article is organized as follows. First, we start by giving a short literature review on existing polymer models. Then, in Section 3, we give a thorough account of the mathematics used to describe the polymer rheology in our proposed model. In Section 3.2 we test the shear thinning part of the model by comparing it to bulk rheology data from Stavland et al. [64]. After this, we summarize the entire viscosity routine with focus on numerical implementation aspects. We apply the simulation model to experimental core flooding data, also from Stavland et al. [64], and we provide a discussion of the results. Finally, we apply the model to a dataset from Howe et al. [28], in which a brine of lower salinity was used compared with the other experiments. Other important elements of the model, such as the computation of in-situ shear rate, inaccessible pore volume effects on polymer transport and reduced apparent viscosity,

as well as a description of the currently implemented temperature and salinity models, are relegated to an Appendix at the back.

2 Overview of previous polymer simulation models

The commercial simulator that is often used as a reference with which to check other simulators, especially in the industry, is Schlumberger's ECLIPSE [20]. According to the official technical description, ECLIPSE 100 currently has more functionality than ECLIPSE 300 with regard to polymer flooding. In the former simulator, the following modelling options have been included:

- A Todd-Langstaff mixing model for handling dispersion at the front edge of a polymer slug, and viscous fingering at the rear edge
- Polymer (instantaneous) adsorption
- A model for permeability reduction, computed in terms of the adsorbed polymer concentration
- Inaccessible (dead) pore volume
- Various temperature effects
- Various salinity effects, e.g., influence of salinity on polymer adsorption
- Various models for handling non-Newtonian polymer rheology

In ECLIPSE 100, the water viscosity can be modified to account for shear thinning and/or shear thickening flow. This can be done by providing viscosity multiplier tables, where the multipliers are specified at a given set of flow rates or, alternatively, shear rates. In the latter situation, the effect of permeability can be more easily accounted for, since the shear rate satisfies $\dot{\gamma} \propto 1/\sqrt{k}$. In the former situation, a different table needs to be specified for each rock type if permeability effects are to be included. ECLIPSE 100 provides an option to model the polymer solution as a Herschel-Bulkley fluid, in which case yield stress effects can be incorporated. When it comes to polymer degradation, ECLIPSE 100 does provide a model for *thermal* degradation. This effect is modelled as a half-life reduction in the polymer concentration. No model for polymer mechanical degradation has been reported implemented in ECLIPSE.

Another well-known commercial reservoir simulatior is CMG STARS [63]. In [24] Hatzignatiou et al. performed simulations using this simulator, in order to test its capabilities with regards to polymer flooding. In [24] no mechanistic models for the polymer viscosity were implemented, and the effects of the different flow regimes were captured by using correlations, in the form of tabular input data, for the effective polymer solution viscosity. The authors concluded that the non-Newtonian behavior of the polymer could be successfully simulated up to certain flow rates, but they experienced numerical issues at the highest flow rates when shear thickening and degradation effects became significant.

The perhaps most well-known research reservoir simulator is the UTCHEM chemical flood simulator [56]. This simulator was originally launched in the late 1970s in order to simulate EOR processes involving surfactants and polymers. Since its inception, the simulator has included a variety of effects, e.g., effects of temperature, inaccessible pore volume, polymer rock adsorption and permeability reduction, as well as a description of how the ionic composition of the brine may alter the polymer intrinsic viscosity. For a long time, the rheology models that were used only incorporated Newtonian and shear thinning flow. However, during the last decade, a more comprehensive polymer model has been implemented in UTCHEM. In 2008, Delshad et al. [17] proposed a unified viscosity model (UVM), in which Newtonian, shear thinning, and shear thickening flow regimes were accounted for. In their work, Delshad et al. used the model to history match data from an earlier work by Masuda et al. [40]. Since then, the model has been extended by various workers from the same research group. For example, in [54] the authors report that more options have been added to the shear thinning and shear thickening rheology models, such as dependencies of the viscosity on polymer concentration. In addition, a model for polymer hydrolysis in porous media was added. According to Sharma et al. [54], the weight-average degree of hydrolysis, D_h, is represented by an additional component (i.e., a "surrogate tracer") in UTCHEM. This component is advected through the grid in the same way as the other components, except that a rate equation has also been implemented in order to track how D_h changes with time, and a tentative relation between D_h and the polymer viscosity has been employed. For more details on the hydrolysis model, see [37]. On the other hand, no models for *mechanical* degradation of polymers have been reported implemented in UTCHEM.

In addition to commercial and proprietary research codes, there has recently been much focus on developing open source tools for reservoir simulation. An example of this is the Open Porous Media (OPM) Initiative [46]. In the long run, these frameworks may become very useful for modelling polymer flooding. However, at the present stage, they do not include functionality that is not also available elsewhere. For example, at the time of this writing, the polymer model implemented in OPM basically includes the same functionality as ECLIPSE 100. To the authors knowledge, none of the freely available source codes include models to handle polymer degradation processes.

In general, relatively few models for polymer degradation have been reported in the reservoir simulation literature. As an example, Sorbie and Roberts [59] presented a model for polymer mechanical degradation that was applied to data from Seright et al. [51]. In their simulations, the polymer

was represented by 20 components, a discrete representation of the molecular weight distribution. Kinetic rate equations were introduced to describe how larger molecular weight fractions were split into smaller ones, and random chain scission was assumed. The model assumed that degradation of a given molecular weight species would only occur above a given, critical value of the local fluid shear/elongational stress (correlated with Darcy velocity). However, the method requires detailed knowledge about the molecular weight distribution, and about the statistics of chain scission. In addition, the number of components needed to accurately model the polymer with such an approach will cause a large increase in the computer running time. Sorbie [60] notes that the model presented in [59] was not strictly predictive, but that it gives a good qualitative description of what can happen when polymer mechanical degradation occurs in porous media. A similar approach was recently taken by Brakstad and Rosenkilde [5], although they assumed the polymers to rupture by midpoint scission. In their model, polymer chain rupture starts at a critical value of the Deborah number, defined as the product of a polymer molecular relaxation time and a porous media effective stretch rate. By introducing an appropriate scaling for the relaxation time, their model predicts that large molecular weight species will degrade into smaller pieces, reducing their mole weight by 50%. The effective stretch rate was in their model calculated as $\dot{\epsilon} = K_f \cdot u/D_p$, where u is the Darcy velocity, D_p is a representative grain diameter (computed from the Blake-Kozeny equation), and K_f is a correction factor to account for different experimental conditions.

A different type of approach was taken by Lange and Huh [36], albeit in the context of modelling thermal degradation of biopolymers. Their model was based on a second-order kinetic rate equation for thermal degradation, assuming random chain scission. In their work, the polymer molecular weight distribution was represented by a single component, representing the weight-average molecular weight.

To sum up, many different effects are included in current polymer flooding simulators, but few simulators include all of the relevant effects. In particular, we would argue that the process of mechanical degradation has been given insufficient attention in the petroleum simulation literature. Additionally, there are a variety of other mechanisms that may be important to consider when interpreting laboratory data, but which are currently not available in most simulation codes, e.g., models for depletion layers of polymers, as well as more elaborate models for permeability reduction. Finally, even in cases where most of these effects are possible to represent using existing tools, the application of the models may require a lot of manual labour and fine-tuning. This is especially the case if different sets of input parameters and/or tables are needed for each rock type in a large field simulation. As such, it is our hope that the model presented herein may lead the way towards better mechanistic models for polymer flooding, and that it can be used to capture the important average flow behavior of polymers in the reservoir.

3 Mathematical model description and preliminary discussion

As mentioned in the introduction, in reservoir simulation, it is common practice to represent the relevant non-Newtonian effects of EOR polymers by means of an apparent aqueous phase viscosity, η, which must in some way be calculated from the velocity obtained from Darcy's law [60]. Moreover, one typically does this by correlating this apparent viscosity to an apparent shear rate in porous media, $\dot{\gamma}$. Then, calculation of η based on the value of the flow rate in a simulation grid block requires the establishment of two mathematical relationships, one between η and $\dot{\gamma}$, and a second one between $\dot{\gamma}$ and the Darcy velocity. We will also adopt this approach. For convenience, we will use interchangeably the terms shear rate and viscosity to denote, respectively, the apparent shear rate and apparent viscosity. In our model, we propose to calculate this viscosity as follows:

$$\eta = \eta_s + (\eta_{sh} - \eta_s) \cdot \eta_{elf} \,. \tag{1}$$

That is, we calculate the total viscosity as consisting of a viscous, shear thinning part, η_{sh}, multiplied with an elongational viscosity factor, η_{elf}. The expression for η_{elf} has been chosen so that, for low shear rates, $\eta \approx \eta_{sh}$, whilst at high shear rates dominated by elongational flow, $\eta \propto \eta_0 \dot{\gamma}^m$, where η_0 is the viscosity at zero shear rate, and m is an empirical parameter determined from experiments. Similar expressions have been used in other simulators reported in the literature, e.g., in [17] they calculate η as the sum of a shear thinning viscosity and an elongational viscosity.

The viscous and elongational contributions to the total viscosity will be further related to the local rock and fluid properties. This will be the topic of the following subsections.

3.1 Shear thinning model: derivation

The shear thinning behavior of EOR polymers can normally be well matched with a Carreau-Yasuda model [2, 71],

$$\frac{\eta_{sh} - \eta_s}{\eta_{sh0} - \eta_s} = (1 + (\lambda_1 \dot{\gamma})^x)^{-n/x} \,, \tag{2}$$

where η_{sh} is the shear thinning viscosity at a given shear rate, $\dot{\gamma}$, and η_{sh0} is the viscosity at zero shear rate (Newtonian regime). The parameter λ_1 is a relaxation time that

determines the onset of shear thinning, and x and $n > 0$ are dimensionless tuning parameters, with x determining the sharpness of the transition from the Newtonian to the shear thinning regime. In terms of the specific viscosity, $\eta_{sp} = \eta_{sh}/\eta_s - 1$, the Carreau-Yasuda equation can be rewritten as

$$\eta_{sp} = \eta_{sp0} \cdot (1 + (\lambda_1 \dot{\gamma})^x)^{-n/x} , \tag{3}$$

which, in the limit of high shear rates, becomes a power-law model in the specific viscosity with slope equal to $-n$. Equation 3 is an empirical model, and the parameters λ_1 and n obtained from matching it with laboratory data will in general be valid only for a specific polymer-solvent combination at a specific temperature, and at a given polymer concentration. Therefore, to reduce the amount of free parameters, it would be of great interest to be able to relate λ_1 and n to other, known parameters in the model.

The shear thinning index, n, in the Carreau-Yasuda expression has experimentally been found to depend on polymer concentration and the intrinsic viscosity [64]. We have suggested a correlation to capture this dependency,

$$n = 1 - \frac{1}{1 + (a_n[\eta]c_p)^{b_n}} = 1 - \frac{1}{1 + (a_n \cdot X)^{b_n}} , \tag{4}$$

where the symbol X is used to denote the product of polymer mass concentration, c_p, and polymer intrinsic viscosity, $[\eta]$. The correlation has been chosen so as to bind n between its physical limits, $n \in [0, 1)$. In Eq. 4, a_n and b_n are constant input parameters for a given polymer, typically obtained from fitting the Carreau-Yasuda model with at least two different polymer concentrations.

A lot of excellent experimental and theoretical work has been done in polymer science to visualize, and to interpret polymeric molecular motion in shear flow. Microscale behavior of DNA molecules has been studied using video fluorescence microscopy, tumbling configurations such as stretch, align, flip, and collapse have been observed [53, 58] and identified as important for the shear thinning flow regime [66]. During the tumbling motion, the polymeric particles spend on average a longer time oriented in the flow directions, and the resulting frictional losses cause shear thinning. In our description of the shear thinning behavior, all the detailed molecular configurations are averaged out, and we are only interested in the characteristic time that determines the transition from Newtonian to shear thinning flow. This characteristic time can be found by considering when the Brownian motion is overcome by the hydrodynamic forces, and in Eq. 2, it corresponds to when $\dot{\gamma} \cdot \lambda_1 \sim 1$. In the present work, we relate λ_1 to a characteristic time scale of rotational diffusion by

$$\lambda_1 = \frac{1}{2D_{rot}} , \tag{5}$$

which is the rotational relaxation time for a rigid object. Equation 5 is the same expression that was suggested by Chauveteau [8] for rigid rod polymers. The diffusion coefficient is computed from the Einstein relations known from statistical mechanics. For describing both rotational and translational diffusion of a Brownian particle immersed in a Newtonian fluid, we use the Einstein-Smoluchowski relation [18],

$$D = \frac{k_B T}{f} , \tag{6}$$

where D is the diffusion coefficient, $k_B T$ is the thermal energy, and f is an appropriate friction factor. Here, k_B is the Boltzmann constant, which has a numerical value of $k_B = 1.38 \cdot 10^{-23}$ J K^{-1} in SI units. For a rotating rigid sphere of radius R immersed in a Newtonian liquid of viscosity η_s, the friction factor in Eq. 6 is $f = 8\pi\eta_s R^3$ [4, p. 95]. By approximating the flexible polymer in solution as a rigid sphere with a given hydrodynamic radius, R_h, we therefore compute the rotational diffusion coefficient according to

$$D_{rot} = \frac{k_B T}{8\pi\eta_s R_h^3} . \tag{7}$$

Inserting (7) into (5) yields

$$\lambda_1 = \frac{4\pi\eta_s {R_h}^3}{k_B T} . \tag{8}$$

Next, we need an expression for the hydrodynamic radius. Before we give the derivation, we list some basic equations and assumptions that are needed for the derivation.

The polymer viscosity is mainly controlled by the intrinsic viscosity, and polymer concentration. The intrinsic viscosity is defined by [26]

$$[\eta] = \lim_{c_p \to 0} \frac{\eta_{sh} - \eta_s}{c_p \eta_s} . \tag{9}$$

The relation between $[\eta]$ and the viscosity-averaged polymer molecular weight M_w is given by the Mark-Houwink equation [21]:

$$[\eta] = K \cdot {M_w}^a . \tag{10}$$

In Eq. 10, K and a are constants, which in general will depend upon the given polymer-solvent pair, and the solution temperature. For random chain polymers in good solvents, typical values of a lie in the range 0.5–0.8 [26].

We use a cubic polynomial to calculate the specific viscosity at zero shear rate, η_{sp0}, in terms of $[\eta]$ and c_p. Specifically, we use

$$\eta_{sp0} = X + k' X^2 + k'' X^3 , \tag{11}$$

where k' and k'' are constants and where, as before, $X = [\eta] \cdot c_p$ denotes the product of polymer intrinsic viscosity, and polymer concentration. The intrinsic viscosity in Eq. 11 is a function of M_w, and the equation captures the main

effect of polymer concentration on the effective viscosity. The equation can further account for the viscosity altering effect of changing the ionic concentrations, by making $[\eta]$ salinity dependent (see Appendix A.4).

The hydrodynamic radius is now calculated by combining the following points:

- Calculate the dense spherical radius of the polymer, R_{sph}, as obtained from the polymer molecular weight and polymer density, ρ_p
- Relate R_h to R_{sph} by introducing a "swelling factor," Φ_{sw}, defined as the ratio between the effective hydrodynamic volume occupied by the polymer and the dense spherical volume, i.e., $\Phi_{sw} = (R_h/R_{sph})^3$
- Obtain an expression for the swelling factor in terms of the polymer intrinsic viscosity

With regards to the latter point, we calculate the swelling factor from the Stokes-Einstein equation for the viscosity of a dilute suspension of solid spheres [49]:

$$\frac{\eta}{\eta_s} = \frac{1+\Phi_h/2}{(1-\Phi_h)^2} \approx (1+2.5\Phi_h)\,. \tag{12}$$

In Eq. 12, Φ_h is the volume concentration of the spheres. In terms of Φ_{sw} as defined above and the mass concentration of polymer, we get:

$$\Phi_h = \Phi_{sw} \cdot \frac{c_p}{\rho_p}\,. \tag{13}$$

Then, by using Einstein's first order approximation, Eq. 12, we get

$$\rho_p \cdot \frac{\eta-\eta_s}{\eta_s c_p} = 2.5 \cdot \Phi_{sw}\,, \tag{14}$$

from which we deduce, by taking the limit $c_p \to 0$:

$$\Phi_{sw} = \frac{[\eta]\cdot\rho_p}{2.5}\,. \tag{15}$$

The dense spherical radius is obtained from the expression

$$\rho_p = \frac{M_w/N_A}{4\pi {R_{sph}}^3/3}\,, \tag{16}$$

where N_A is Avogadros' number. Thus

$$R_h^3 = \frac{3}{4\pi N_A \rho_p} \cdot \Phi_{sw} \cdot M_w\,, \tag{17}$$

and by combining Eqs. 15 and 17, we finally obtain

$$R_h = \left(\frac{3}{10\pi N_A}\right)^{1/3} \cdot ([\eta]\cdot M_w)^{1/3}\,. \tag{18}$$

We note that expression (18) is the same as the one given in, e.g., [27], when making the proper unit conversions. It is also commonly seen in various textbooks. Combining Eqs. 8 and 18, the rotational relaxation time can finally be calculated as

$$\lambda_1 = \frac{6}{5R_g} \cdot \frac{\eta_s [\eta] M_w}{T}\,, \tag{19}$$

where $R_g = k_B \cdot N_A$ is the ideal gas constant. Note that this time constant is equal to the one predicted by the FENE dumbbell model. In the FENE model the factor 6/5 is replaced by $(b+5)/b$, thus in our model $b = 25$, which fits well with experimental observations where b is reported to be in the range [10, 100] (see e.g. Bird et al. [3, p. 81]). In Eq. 19, to account for the gradual increased relaxation time caused by interaction forces between polymer molecules at higher concentrations, we replace $[\eta]$ with the first order approximation:

$$[\eta] \approx \frac{\eta_{sp0}}{c_p}\,. \tag{20}$$

Thus, the final expression used in the simulation model becomes

$$\lambda_1 = \lambda_a \cdot \frac{\eta_s \eta_{sp0} M_w}{c_p T}\,, \tag{21}$$

where the prefactor λ_a, having a theoretical value of $\lambda_a = 0.144\ \mathrm{K\ mol^{-1}\ J^{-1}}$, is used as a tuning parameter to account for approximations in the derivation by assuming spherical shape, and by ignoring shear deformation of the polymer body. Also, uncertainty in the molecular weight and eventual effects of polydispersivity will affect the value of λ_a. Equation 21 provides a scaling of the rotational relaxation time which can be used to generate different shear thinning viscosity curves as a function of the local polymer properties. This scaling group is the same as in the Rouse relaxation time for dilute solutions presented in [8]. The remaining input parameters required to calculate the shear thinning viscosity—k', k'', K, and a—may be varied among different polymers, but they should be known from bulk rheology measurements.

3.2 Shear thinning model versus bulk rheology data

The shear thinning model was matched with bulk rheology data for some of the HPAM polymers investigated in Stavland et al. [64]. The polymers are listed in Table 1 using a four-digit name indicating their molecular weight (two first digits) and hydrolysis degree (two last digits), e.g., 2030 indicates an average molecular weight of 20 MDa, with 30% degree of hydrolysis. The commercial names of the polymers have also peen provided in the table. For most polymer types the data were recorded at 7 different concentrations in the range from 250 ppm to 5000 ppm, and at shear rates from 0.1 to 500 $\mathrm{s^{-1}}$.

The model parameters were estimated, for one polymer at the time, by minimizing the sum of squared relative error between calculated and measured specific viscosity for all datapoints covering variation in concentration and shear rate. The minimization was first done with a minimum of constraints. The expression for the shear thinning index,

Table 1 Matched parameters for the shear thinning model, as well as calculated zero shear thinning exponents, shear viscosities, and polymer relaxation times for the bulk solution

Polymer	M_w	$[\eta]$	k'	k''	λ_a	a_n	b_n	x	n	η_0	λ_1	ϕ_1	λ_2
530 (3230S)	5	1467	0.01	0.12	0.722	0.063	0.804	1	0.170	4.86	0.031	0.21	0.00103
1030 (3430S)	10	2275	0.22	0.049	0.803	0.063	0.804	2	0.225	9.58	0.155	0.218	0.00335
1530 (3530S)	15	2424	0.247	0.091	0.306	0.078	0.56	1	0.331	13.18	0.126	0.177	0.00413
2030 (3630S)	20	3750	0.01	0.077	0.350	0.063	0.804	1	0.303	22.17	0.336	0.223	0.01138
Howe et al. [28]	3.6-31		0.247	0.178	0.450	0.078	0.505	1.1					

In addition, the critical time scale λ_2 has been calculated, at porosity $\phi = \phi_1$. All the simulated HPAM polymers from SNF Floerger had a reported hydrolysis degree of 30%, and the Mark-Houwink exponent was set to $a = 0.6$ for all four polymers. The injected polymer concentration was 1500 ppm in all of the core experiments from Stavland et al. [64]. Also included is the input parameters used to match bulk viscosity data from Howe et al. [28]. The dimensional quantities listed in the table have the following units: $[M_w]$ = MDa, $[\eta]$ = ml g^{-1}, $[\lambda_a]$ = K mol^{-1} J^{-1}, $[\eta_0]$ = mPas, $[\lambda_1] = [\lambda_2]$ = s

Eq. 4, was fitted to the result in the left plot of Fig. 1. Then, the minimization was repeated with fixed shear thinning index parameters.

In the right plot of Fig. 1, we see the matched values of λ_1 versus the scaling group $X_c = \eta_s \eta_{sp0} M_w / c_p T$ on a log-log plot, see Eq. 21. The line in the figure indicates a constant λ_a parameter that matches the higher λ_1-values. However, using λ_a individually matched for each polymer type (see Table 1) resulted in a slightly better match to the simulated coreflood experiments presented later.

3.3 Shear thickening model: background

In straight uniform conduits and steady-state flow, polymers tend to display a shear thinning behavior. In contrast, in a porous medium, the apparent viscosity at high shear rates has frequently been observed to increase with shear rate. Similar behavior has also been seen in capillary tubes with an abrupt contraction, as well as in channels with varying cross-sections [6, 8, 9]. For the case of capillary tubes, it has been argued that the increased flow resistance is caused mainly by the sharp acceleration at the entry point of the tube, due to the abrupt change in the diameter at the capillary entrance [1, 8].

This effect, which is commonly referred to as (apparent) shear thickening in the petroleum literature, is related to the elastic nature of the polymers. The flow of polymeric liquids is coupled through tensor constitutive equations to the local flow field in the pore space, and time-dependent flow and non-uniform pore geometries give rise to a non-trivial relation between flow rates and pressure drops. It has been common to link shear thickening behavior to the notion of the coil-stretch transition [16], and to explain the increased flow resistance in terms of extensional viscosity, i.e., as an effect due to elongation and contraction of the polymer molecules in the flow field [9, 17]. However, uncovering the exact mechanisms responsible for the increased macroscopic flow resistance is an active area of research. With the development of microfluidic techniques it is now possible to observe directly the response of individual polymer molecules to extensional flow, as well as to visualize the flow field streamlines [25, 29, 50]. Using these techniques,

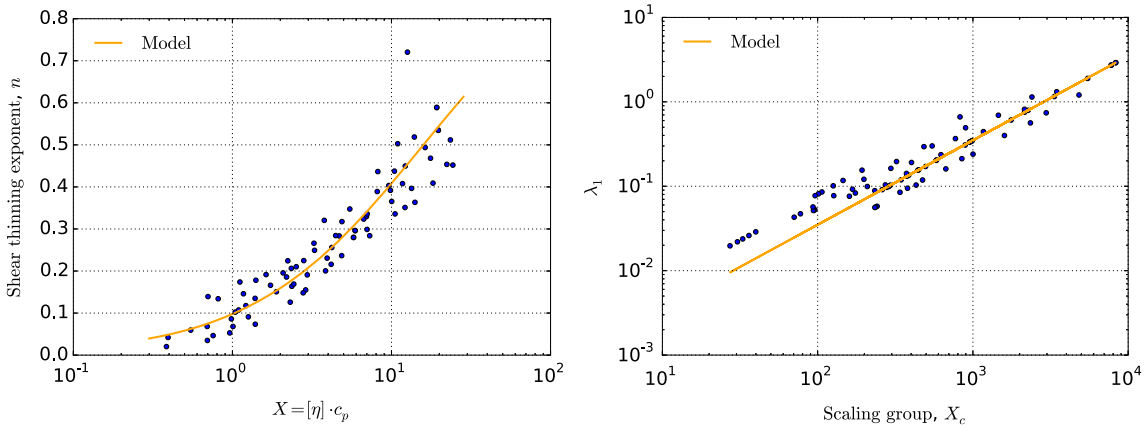

Fig. 1 Left: Shear thinning index n obtained for the dataset fitted with $a_n = 0.063$ and $b_n = 0.804$. Right: λ_1 from the second match, plotted versus the scaling group $X_c = \eta_s \eta_{sp0} M_w / c_p T$. The line represents the model with $\lambda_a = 0.350$ K mol^{-1} J^{-1}

an alternative explanation in terms of time-dependent elastic instabilities has been proposed [28, 33, 38].

In any event, and as we stressed in Section 3.1 when discussing the shear thinning model, we are here mainly concerned with obtaining useful scaling groups that can be implemented to simulate polymer flooding in a standard reservoir simulator. We therefore wish to estimate a critical shear rate at which shear thickening flow is first observed. In our model we calculate this critical rate as the inverse of λ_2, where λ_2 is a characteristic time scale that depends on both the rock and fluid properties. In the literature, the onset of apparent shear thickening behavior has often been correlated with the dimensionless Deborah number [17, 23, 40], N_{De}. It is defined as

$$N_{De} = \frac{\tau_{el}}{\tau_r}, \tag{22}$$

where τ_{el} is a characteristic time scale for the polymer, and where τ_r is a typical time scale of observation. Herein, we define τ_r as an average residence time of the polymer in the rock. For homogeneous, extensional flow fields the coil-stretch transition has been predicted to occur at a critical value of the Deborah number, $N^{\star}_{De} = 0.5$ [47, 57]. However, in our model for porous media flow, we introduce $N^{\star}_{De}$ as a fitting parameter, to be obtained from a match between modelled and experimental values of λ_2. The procedure that was used to obtain an expression for λ_2 can be outlined as follows:

- Compute the "elongational relaxation time" for the polymer, τ_{el}, which is the time it takes for the polymer to diffuse a length equal to its effective size in solution
- Compute an average pore residence time for the polymer in the rock, τ_r, using the Kozeny-Carman equation. This residence time is used as the time scale of observation in the calculation of N_{De}
- The onset of shear thickening is assumed to happen when the polymer relaxation time is of the same order of magnitude as the residence time, e.g., when $N_{De} = N^{\star}_{De} \approx 1$ [8, 9]
- Use the previous considerations to derive a critical shear rate for the onset of shear thickening, $\dot{\gamma}_c$, and define $\lambda_2 = 1/\dot{\gamma}_c$

We may note that this use of N_{De} does not describe the actual onset of elongation at pore entrances, but rather the situation where the polymer molecule has insufficient relaxation time to recover from its distortion in the previous pore throat before entering the next. We assume that these events are close in time, and that the shear thickening effect of the initial elongation, if significant, can be accounted for by reducing $N^{\star}_{De}$ with a factor which is fairly independent of permeability.

Details on the derivation of the characteristic time, λ_2, is provided in Section 3.4. Once it has been obtained, the elongational viscosity factor, η_{elf}, is calculated according to

$$\eta_{elf} = (1 + (\lambda_2\dot{\gamma})^{x_2})^{\frac{m+n}{x_2}}, \tag{23}$$

where x_2 is a tuning parameter for the transition to the new flow regime, and m is an exponent fitting parameter. The motivation for the model can be seen from Fig. 2.

In this figure, we have plotted the logarithm of the apparent specific viscosity of a polymer solution versus the logarithm of the in-situ porous media shear rate, using data from one of the serial core experiments reported by Stavland et al. [64]. From the figure, the graph looks approximately linear for shear rates following the onset of shear thickening, and it can therefore be described by a power-law scaling. A combination of formulas (1), (2), and (23) yields

$$\eta_{sp} = \eta_{sp0} \cdot \frac{(1 + (\lambda_2\dot{\gamma})^{x_2})^{(m+n)/x_2}}{(1 + (\lambda_1\dot{\gamma})^{x})^{n/x}}, \tag{24}$$

which for $\lambda_2\dot{\gamma} \gg 1$ predicts that $\eta_{sp} \propto \dot{\gamma}^m$, i.e., that $\log \eta_{sp}$ is a linear function of $\log \dot{\gamma}$ with slope m. The plot in Fig. 2 was typical for all experiments investigated, and the estimated maximum slope m in the shear thickening region was for all cases determined as $m = 1.5 \pm 0.2$. (11 samples). The maximum slope of the declining part (purple line in Fig. 2) was 0.49 ± 0.09. The intersection point between the two straight lines in Fig. 2 can be interpreted as the critical point for the onset of polymer degradation in the core experiments. Note that the results in the figure represent average properties integrated over the length of the core plug, and we expect the indicated critical point to depend on the core

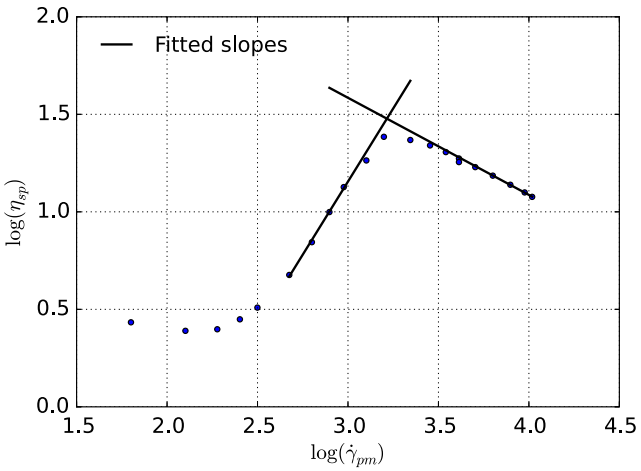

Fig. 2 In-situ rheology of the 1030 polymer in a 0.299 D Berea sandstone core. The slope of the increasing line, which represents the maximum slope in the shear thickening region, was found to be $m = 1.5$. Note that this plot represents averaged parameters, i.e., it is based on measured pressure drops across a full column of length $L \approx 7.0$ cm. The effective shear rate in porous media, $\dot{\gamma}_{pm}$, was calculated according to Eq. 50

length. However, since all investigated core plugs were of the same length (7 cm), some interesting observations can be made by comparing the critical points from all the core tests. The core tests cover variations in permeability from 137 to 2019 mD, and in polymer molecular weight from 5-20 MDa. The average shear rate at the critical point (9 samples, two outliers removed) was $1480 \pm 550\ \mathrm{s}^{-1}$, while average shear stress, calculated as $\tau = \dot{\gamma} \cdot \eta$, was 54 ± 5 Pa. These correlations with the critical point strongly indicate that shear stress rather than shear rate governs the mechanical degradation. The tests compared here are all from the first core in the dual core experimental setup. Results for the second core essentially overlap the results for the first core in the elongation region, while the declining part shows a parallel shift downwards.

3.4 Shear thickening model: derivation of λ_2

To compute the pore residence time in Eq. 22, we assume a pore length L_p equal to the characteristic grain size D_g of the medium obtained from a Kozeny-Carman equation. The Kozeny-Carman approach consists in converting from a capillary tube representation of the porous medium to a medium of spherical grains by preserving the medium surface area, S_A. The relation between the effective pore radius R_p and effective grain size is $S_A = 2\phi/R_p = 6(1-\phi)/D_g$ [35]. Then, we can write

$$\frac{L_p}{R_p} = 3 \cdot \frac{1-\phi}{\phi}\,, \tag{25}$$

where ϕ is the porosity. The residence time can therefore be computed as

$$\tau_r = \frac{L_p}{v_p} = 12 \cdot \frac{1-\phi}{\phi\dot{\gamma}}\,, \tag{26}$$

where $\dot{\gamma} = 4v_p/R_p$ relates the shear rate at the wall to the average pore velocity v_p in the capillary tube representation.

The elongational relaxation time is calculated as a characteristic time scale of diffusion,

$$\tau_{el} = \frac{(2R_h)^2}{D_t} = \frac{4R_h^2}{D_t}\,, \tag{27}$$

where R_h is the hydrodynamic radius, and D_t is a translational diffusion coefficient determined from the well known Stokes-Einstein equation [8]:

$$D_t = \frac{k_B T}{f} = \frac{k_B T}{6\pi\eta_s R_h}\,. \tag{28}$$

Combining (18) with (27) and (28), we calculate

$$\tau_{el} = \frac{36}{5} \cdot \frac{\eta_s[\eta]M_w}{R_g T}\,. \tag{29}$$

We then calculate λ_2 according to $\lambda_2 = 1/\dot{\gamma}_c$, where $\dot{\gamma}_c$ is the shear rate at which $N_{De} = N^{\star}_{De}$. By combining Eqs. 18, 22, 26, and 29, we end up with the following expression for λ_2:

$$\lambda_2 = \frac{1}{N^{\star}_{De}} \cdot \frac{3}{5R_g} \cdot \frac{\phi}{1-\phi} \cdot \frac{\eta_s[\eta]M_w}{T}\,. \tag{30}$$

In the present case, we found that $N^{\star}_{De} = 0.5$ provided a good fit of the model for all the experimental data. Note that the estimated $N^{\star}_{De}$, representing an average value for the porous medium, will depend on the tuning parameter α_c used for calculating average in situ shear rate (see Table 2). As with λ_1, the formula for λ_2 can be used to generate different viscosity curves for the shear thickening regime under varying reservoir conditions, and for different polymers. The situation at higher rates ($N_{De} \gg N^{\star}_{De}$), when the polymer chains are already stretched before entering contractions, is represented by the empirical exponent m from experiments, see Eqs. 23 and 24.

3.5 Polymer degradation model: background

As the flow rate is increased further beyond the critical rate for onset of shear thickening, experiments indicate that the viscosity reaches a "maximum level," after which there is a sharp decline in viscosity at yet higher rates, see Fig. 2. This is because of polymer mechanical degradation in porous media. At sufficiently high stresses, covalent bonds along the polymer chain backbone will break, causing a reduction in the effective molecular weight and apparent viscosity. It has been observed that this chain scission happens more rapidly for polymers with higher molecular weights. Indeed, multiple investigators have reported that for polymers in extensional flow fields, the onset of polymer mechanical degradation seems to occur at a critical strain rate (for a given system), $\dot{\epsilon}_f$, that scales as a power-law with the weight-average polymer molecular weight [6, 19, 34, 42, 44, 69]:

$$\dot{\epsilon}_f \propto M_w^{-\xi}\,. \tag{31}$$

This power-law scaling has been found for both turbulent and laminar flows, although the numerical value of the scaling exponent can vary depending on the flow geometry, as well on differences in solvent quality [68]. In the literature, there has been considerable debate as to how the obtained scaling exponents can be rationalized from more fundamental physics, i.e., in terms of polymer kinetic theory. One central issue concerns the precise mechanism of polymer chain cleavage. For example, one can ask whether the polymer chains rupture preferentially near the midpoint of the chains, or whether the process is more random?

Table 2 Model input parameters that were kept fixed in all cases

Parameter	Value	Explanation
IPV_0	0.1	Inaccessible pore volume (constant part)
f_{dpl}	1.0	Tuning parameter used in depletion layer model
f_{rkf}	1.0	Tuning parameter for size of adsorbed layer
$C = (L_t/L)^2$	3.0	Tortuosity factor
α_c	2.0	Tuning parameter used in the shear rate calculation
$N^{\star}_{De}$	0.5	Tuning parameter for calculating λ_2 (critical Deborah number)
m	1.5	Slope parameter for the shear thickening model
x_2	3.0	Governs the sharpness of the transition to the shear thickening regime
r_{deg}	0.0015	Rate constant used in degradation model
α_d	3.0	Degradation dependency on shear stress
β_d	1.0	Degradation dependency on molecular weight
λ_3	$1/8 \cdot \lambda_2$	Determines the onset of reduced swelling of adsorbed polymer
n_3	1.0	Exponent used in the shear dependent permeability reduction model
x_3	4.0	Parameter used in the shear dependent permeability reduction model

Note that the value for the rate constant, r_{deg}, listed here is based on Eq. 33 with τ in units of Pa, R_p in μm, and M_w in MDa

In the polymer science literature, it has been common to distinguish between two types of extensional flow:

- Quasi steady state flow (QSSF), characterized by a flow field that is "purely" elongational in nature, e.g., flow near a stagnation point where the polymer residence time is very large
- Fast transient flow (FTF), characterized by a short residence time (e.g., capillary entrance flows)

A common explanation for the differences in calculated scaling exponents for $\dot{\epsilon}_f$ has been that the mechanism for chain scission is different in the two types of flow [14]. For QSSF flows, it is argued, the polymer molecules stretch to more or less full extension, before breaking near the middle where the tension is greatest [44]. On the other hand, for FTF flows the polymer residence time is too short to obtain full extension, and it has been assumed that the polymer breaks while in a partially stretched state. However, even for such flows midchain scission have been inferred [43], which has been difficult to reconcile with fundamental models for the polymer chain. In general, there seems to be little consensus on this topic, and alternative explanations have been proposed to account for the different chain scission exponents [31]. For example, Islam et al. [31] and Vanapalli et al. [69] have made the argument that the discrepancy may equally well be explained by differences in the Reynolds number at which the experiments were conducted. They claim that many experiments previously thought to having been performed under laminar conditions were, in fact, influenced by turbulence.

Of course, for flows in porous media, the situation is much more complex than in highly idealized experimental setups investigated in the laboratory. In porous media, the polymer will travel through a complex network of pores, of varying pore sizes, and with rapid variations in the effective, cross-sectional area available to flow. This results in a mixed flow, where both elongational and shearing components contribute to the flow field. Even so, based on coreflooding data such as Fig. 2, it seems that the onset of degradation can be correlated with a critical shear rate in the porous medium. As we discussed in Section 3.3, this shear rate is a system-dependent parameter with a value can vary greatly from case to case. Based on our data, we calculated that the onset of degradation happened at relatively constant values of shear stress, defined as $\tau = \eta \cdot \dot{\gamma}$, where η and $\dot{\gamma}$ are the averaged apparent viscosity and shear rate, respectively, for the core samples investigated. In terms of the capillary tube representation of the porous medium, τ represents the shear stress at the wall of the capillary tube.

Based on these observations, we assume in our model that most of the degradation takes place close to the rock surface, where the shear force is large, and that it decreases away from the surface where τ is lower. While this assumption is dictated by macroscale observations in cores with different permeabilities, a simplified microscale picture could be that while polymer molecules at the flow centre line will be exposed to elongational forces alone, polymer molecules closer to the surface may be exposed to shear forces in addition to elongational forces. To incorporate these mechanisms in the model, the degradation rate is taken to be proportional to the rock specific surface area, which is $S_0 =$ rock surface/pore volume $= 2/R_p$ for the capillary tube representation of the porous medium. The implication of this term is that at a given shear stress, and for rocks of

different permeability, the polymer will degrade faster in the low permeable rock with smaller effective pore radius, see Eq. 51.

3.6 Polymer degradation model: implementation

We model the mechanical shear degradation by introducing a parameter f_{rup}, which can be considered as the fraction of polymer molecules that rupture per time unit, or as the probability for chain rupture. At the end of a transport timestep in the simulation, the molecular weight is updated according to the differential equation

$$\frac{dM_w}{dt} = -M_w \cdot f_{rup} \,. \tag{32}$$

We calculate f_{rup} according to

$$f_{rup} = (r_{deg} \cdot \tau)^{\alpha_d} \cdot \frac{2M_w^{\beta_d}}{R_p} \,, \tag{33}$$

where r_{deg} is a rate constant. The rationale for using expression (33) can be summarized as follows:

- Intuitively, below a certain treshold of stress, little or no degradation should happen, whereas at and above a certain "critical" level the degradation process should accelerate. This is captured by the term involving τ and the exponent $\alpha_d > 1$
- The term $2/R_p$ is the specific surface area, as discussed above
- Longer polymer chains should have a larger probability of breaking [6, 14, 32]. This is captured by the $M_w^{\beta_d}$ term

To summarize, Eq. 33 predicts more degradation at higher shear stress, at lower permeability, and for larger molecular weight polymers.

A novel feature of the proposed approach is that the polymer is represented by two components in the simulator:

1. A volumetric polymer concentration, c_p/ρ_p (recall that c_p is the mass concentration), and
2. A molar polymer concentration, c_{mol} (e.g. mol l^{-1}).

That is, we do not attempt to explicitly model the molecular weight distribution, but rather use a single component, in addition to the mass concentration of polymer, to keep track of how the molecular weight changes inside the reservoir. It should be noted that the actual target for the model is to keep track of the viscous properties of the degraded polymer, and that the computed molecular weight is related to intrinsic viscosity using the same Mark Houwink exponent a, given as input, throughout the simulation (10).

Equations 32 and 33 establish a mathematical relation between the porous medium effective shear rate, and the molecule rupturing rate. The result is an increased molar concentration and a corresponding reduction in molecular weight since the volumetric concentration is unchanged. In consistent units:

$$c_{mol} = \frac{c_p}{M_w} \,. \tag{34}$$

Once a new value for M_w has been found, the intrinsic viscosity is updated from the Mark-Houwink Eq. 10. More details concerning the numerical solution of Eq. 32 are provided in Section 4.

3.7 Polymer adsorption and residual resistance factor

Here, we describe the polymer adsorption model used in the simulations. We only use this adsorption model to generate simulated permeability reduction factors, computed from adsorbed polymer, similar to measured values (RRF defined below). No measurements of adsorption were available from the experiments. Although polymer adsorption is reversible, or at least partly reversible, and may change if conditions are changed, processes like desorption or redistribution of already adsorbed polymer due to altered conditions are known to be very slow and may in many cases be neglected (see Zhang and Seright [72]). Therefore, we assume adsorption to be constant and irreversible throughout the experiments. Mathematically, we describe the adsorption by a Langmuir isotherm:

$$A_p = \frac{bc_p Q_m}{1 + bc_p} \,. \tag{35}$$

In Eq. 35, A_p is the polymer concentration adsorbed on the rock and Q_m is the maximum adsorption capacity, both expressed as a fraction of the total pore volume. The parameter b determines how fast the adsorption occurs, i.e., at which polymer concentration the plateau, $A_p = Q_m$, is reached. Polymer adsorption can lead to permeability reduction, which is typically quantified in corefloods by introducing the residual resistance factor, RRF. The latter quantity is defined as

$$RRF = \frac{k_{wi}}{k_{wf}} \,, \tag{36}$$

where k_{wi} is the initial permeability to water before polymer injection, and k_{wf} is the post-flush water permeability. We have tested two models for relating RRF to the adsorbed amount of polymer, which we introduce shortly here (see Appendix A.3 for more details). Let A_{pt} denote the effective volume fraction of the total pore space that is occupied with adsorbed polymer. We then compute RRF according to

$$RRF = \frac{1}{(1 - A_{pt})^2} \,. \tag{37}$$

In model I, which is independent of shear rate, we compute A_{pt} as

$$A_{pt}^{I} = f_{rkf} \cdot \frac{A_p \Phi_{sw}}{(1 - IPV_0)}, \tag{38}$$

where Φ_{sw} is the swelling factor defined in Eq. 15 computed from the molecular weight of adsorbed polymer, which can differ significantly from M_w in solution. Equation 38 models the extension of adsorbed polymer molecules into the solution. The term IPV_0 is the fraction of the pore volume that is totally inaccessible to the polymer (see Appendix A.1), and f_{rkf} is included as a tuning parameter. The investigated dataset provides no information about adsorbed polymer, so in the simulations we used $f_{rkf} = 1$ and adjusted Q_m to approximate experimental RRF.

Model II should be regarded as a test of one possible method which can improve the match of experimental effluent viscosity (see the section on simulation results). In this model, A_{pt} is made a function of shear rate. We have tested the following expression:

$$A_{pt}^{II} = f_{rkf} \cdot \frac{A_p}{(1 - IPV_0)} \cdot ((\Phi_{sw} - 1) f_{sh} + 1) . \tag{39}$$

For simplicity, we relate f_{sh} to a time constant in the same way as for the shear thinning and shear thickening viscosities:

$$f_{sh} = (1 + (\lambda_3 \dot{\gamma})^{x_3})^{-n_3/x_3} . \tag{40}$$

That is, at low flow rates we will have $f_{sh} \approx 1.0$, and polymer molecules adsorbed at the pore wall extend fully into the solution. On the other hand, as the flow rate increases, more and more of the polymer will be forced closer towards the surface, resulting in less pore blocking. In formula (40), x_3 and n_3 are constants, and we take λ_3 to be proportional to λ_2. Moreover, we assume that the onset of this effect happens at a higher shear rate than the critical shear rate for the onset of shear thickening, i.e., that $\lambda_2 > \lambda_3$. For the simulations presented in this paper, we have used $\lambda_2/\lambda_3 = 8$.

4 Numerical solution of the polymer model

We have implemented the polymer viscosity model in an in-house simulator at IRIS, IORCoreSim. This simulator, which is written in C++, has the capability to simulate a variety of EOR processes for two-phase flow in porous media. The main flow field is obtained from a finite-difference discretization, using a sequential solution method to compute the phase pressures and saturations for the oil and water phases [62, 70]. First, the pressure fields are calculated using a linear pressure equation, keeping the saturation dependent variables fixed at their values from the previous timestep. Next, the velocities of the water and oil phases that were computed during the first step are updated by solving an additional saturation equation for the water saturation. This saturation equation is formulated in terms of the fractional flow of water, and it is solved implicitly with respect to the saturation dependent variables, k_r (relative permeability) and p_c (capillary pressure), while keeping the total flowrate from the pressure solution fixed.

Once the flow field has been obtained for a global timestep, the transport of the individual species, in this case the brine and polymer components, is performed explicitly using operator splitting. First, the total concentration of polymer is updated in each grid cell. Next, polymer adsorption is computed, followed by an update of the solution viscosity and the RRF factor. The viscosity algorithm used for a grid block during a transport timestep, Δt, can be roughly summarized as follows:

1. Compute in situ shear rate using current flowrate and RRF from the previous timestep
2. Calculate an initial value for the viscosity-averaged polymer molecular weight, M_w^0, based on the newly updated molar and volumetric concentrations, see Eq. 34
3. Compute the intrinsic viscosity in terms of the updated M_w and the effective salinity of the brine (see Appendix A.4)
4. Find the polymer concentration to be used in the viscosity calculations (correct for inaccessible pore volume, including depletion layer, see Appendix A.1), and calculate polymer apparent viscosity as a function of polymer concentration, shear rate, and depletion layer
5. Add the effect of elongation
6. The degradation is solved implicit in time with respect to M_w, by employing an iterative algorithm where in each iteration the full viscosity model is calculated. The initial value for M_w estimated in step 2 is used as a starting point
7. If adsorption is included, calculate RRF

The crucial step that necessitates an iteration loop is the solution of Eq. 32. This is because most of the parameters in the model are functions of M_w. We discretize (32) as

$$M_w = \frac{M_w^0}{1 + \Delta t \cdot f_{rup}(M_w)}, \tag{41}$$

where M_w^0 is the molecular weight before degradation is included, and M_w represents the unknown value when degradation over the last time step is included. We solve (41) using a modified false position ("regula falsi") chord method, also known as an "Illinois-type" method [22].

5 Simulation results from experiments in synthetic sea water (SSW)

5.1 Experimental background and simulation procedure

We applied the model to some of the experiments reported by Stavland et al. [64]. The selected experiments cover variations in molecular weight from 5 to 20 MDa, and in permeability from 137 and 2019 mD. The hydrolysis degree was the same, 30%, for all the polymers. The experiments were designed to investigate the apparent shear thickening and degradation flow regimes. Model parameters for the Newtonian and shear thinning regimes were matched to bulk viscosity measurements for each polymer, see Table 1. The adsorption capacities were adjusted to obtain RRF factors close to the experimental values, but the values listed (Table 5) are consistent with what would be expected from variation in permeability. The rest of the model parameters describing elongation and degradation were kept fixed among all cases (Table 2). For all simulations, we compared predicted resistance factors, RF, to the ones obtained from the experimental data. The resistance factor, or mobility reduction factor, is defined by

$$RF = \frac{\lambda_w}{\lambda_p} = \frac{\Delta p}{\Delta p_w}\,. \tag{42}$$

That is, RF is the ratio of the water mobility prior to polymer injection, $\lambda_w = k_{wi}/\eta_s$, to the polymer mobility at the same rate, $\lambda_p = k_p/\eta$. If the residual resistance factor, Eq. 36, can be considered a constant for a given medium, we obtain the following relation between RRF and RF:

$$RF = \frac{\eta}{\eta_s} \cdot RRF = \eta_{rel} \cdot RRF\,. \tag{43}$$

All the investigated polymers were mixed with synthetic sea water (SSW), with ionic concentrations reported in Table 3. As a result, we could represent the brine by a single component, using a constant viscosity of $\eta_s = 1.07$ mPa s at room temperature, $T = 20$ °C. The polymer-brine solutions were injected into different serial mounted sandstone cores, with properties given in Table 4. All of the cores were cylindrical, with a length of approximately 7 cm, a diameter of 3.8 cm, and a porosity close to 20%. The solutions were flooded at a variety of rates, and steady state differential pressures were recorded over both cores, which we will denote by Core 1 and Core 2, respectively. The polymer solutions were injected at a polymer concentration of 1500 ppm.

Table 3 Make-up of the synthetic seawater, SSW

Salt	Concentration [g l^{-1}]
NaCl	23.495
KCl	0.746
$MgCl_2 \cdot 6H_2O$	9.149
$CaCl_2 \cdot 2H_2O$	1.911
Na_2SO_4	3.408
$NaHCO_3$	0.168

We simulate the experiments starting with the experimental initial rate because, in some of the experiments, the initial rate seemed to be in the lower end of the degradation regime, which affects the molecular weight of adsorbed polymer, and consequently RRF. After that, the injection rate was stepwise increased from low to high value, and finally a post-polymer water injection was simulated. Simulated values of in particular RF, but also shear rate and RRF, showed decreasing trends from the inlet to the outlet end of the core. Therefore, to compare simulation with experiment, these properties are computed in the same way as for the experiments, using the total pressure drop across the core and the flowrate. RRF is first calculated based on the simulation of a post-polymer water injection. Then, for each flowrate, RF and η are obtained using the Eqs. 42 and 43, while the shear rate is computed from Eq. 50.

In addition to estimating RF and RRF factors, polymer samples were collected at the effluent, at different injection rates. These samples were subsequently analyzed in a rheometer at a low shear rate, to characterize the extent of degradation.

5.2 Models for permeability reduction

Initially, we matched the experimental RF profiles by tuning the degradation model and assuming constant RRF, model I (38). Although good reproduction of RF values were obtained at all flow rates, computed viscosities using simulated effluent molecular weights were substantially lower than the experimental values, as can be seen from Fig. 3. Since RF is a product of viscosity and RRF, Eq. 43, the intuitive idea is that if viscosity is higher, RRF must be reduced to obtain the same RF value. This was the motivation for introducing model II with rate dependent RRF, Eq. 39. The difference between the two models is illustrated in Fig. 3, where we have compared the experimentally determined effluent viscosities with values predicted from the simulator for the 1530 polymer.

The shear rate dependent model (model II) is able to reproduce both effluent polymer properties (Fig. 3) and RF satisfactory (shown later). We conclude that rate-dependent RRF is a good candidate for explaining what goes on inside the core. However, we note that the theory of decreased permeability reduction at higher flow rates seems to contradict experimental data reported in the literature [13, 30]. For example, several authors have reported an increase in

Table 4 Properties for the various dual core systems

System id	Rock type	L_1	L_2	k_1	k_2	ϕ_1	ϕ_2
1	Berea	7.2	7.1	414.61	305.63	0.21	0.22
2	Berea	7.1	7.1	298.5	291	0.218	0.216
3	Berea	7	7	721.7	612.8	0.223	0.213
4	Berea	7.2	7.2	161.3	136.9	0.177	0.176
5	Berea	7.0	7.0	823.6	800.4	0.223	0.213
6	Bentheim	7.1	7.1	2018.8	1998.1	0.235	0.235
Howe et al. [28]	Bentheim	5		3100		0.23	

The diameter was in all cases $d = 3.8$ cm, while the lengths, permeabilities and porosities are denoted by L_i [cm], k_i [mD], and ϕ_i, for cores with indices $i = 1, 2$. Also included is core data from experiments reported by Howe et al. [28]

the permeability reduction at higher flow rates, which they explain as a consequence of more polymer molecules being adsorbed on the surface at the higher flow rates due to an increase in the hydrodynamic forces.

Another possible explanation for the effluent viscosity disrepancy, which remains to be tested, is the choice of the Mark-Houwink exponent, a, from Eq. 10. By decreasing a, the polymer will lose less of its viscosity when degraded. The polymer will be degraded more (to a lower M_w), but may still result in an increased effluent viscosity. Furthermore, an important question to ask is how polymer degradation will alter the molecular weight distribution of the polymer. If the shape of the distribution is heavily altered, it is possible that the relation between $[\eta]$ and M_w which was originally used may no longer be valid after degradation. Another issue is that the rationale for the polymer degradation model, Eqs. 32 and 33, were implicitly

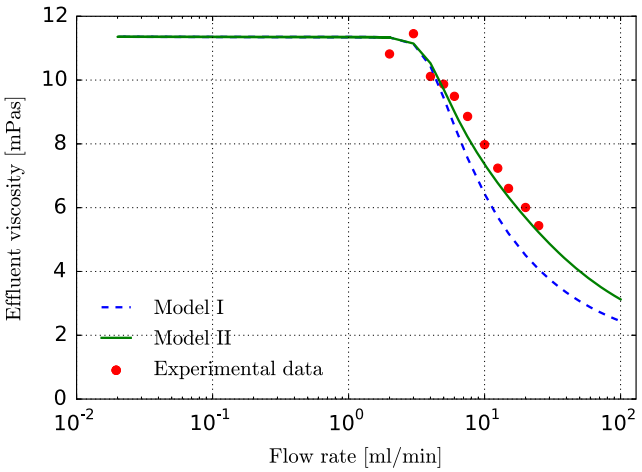

Fig. 3 Effluent viscosities for the 1530 polymer, measured from bulk samples collected at the effluent. The data are taken for the case where Core 1 and Core 2 had permeabilities of 721.7 mD and 612.8 mD, respectively. The red dots are experimental datapoints, whilst the solid line was obtained from the match with the model for shear dependent permeability, model II. The dashed lines represent the shear independent model, model I

based on a conception of M_w as the number average molecular weight, M_n, in that we considered the fraction of polymer molecules expected to rupture. However, the mass and viscosity averages will be quite different from M_n for a polydisperse sample.

It should also be remarked that there are several experimental uncertainties that can make a proper estimation of the residual resistance factor difficult, such as excess pressure drops being measured during the post-polymer phase [52]. Another issue, which may potentially be misleading, is that the RRF factor may not be a constant at all, but may rather depend on the applied flow rate. This is what we have explored with our model II. However, we remark that a predictive simulator needs to take the permeability reduction effect into account, as it would otherwise be impossible to match the observed pressure drops. The same applies to several of the other mechanisms included in the simulator. What is important for us here, in order to properly compare theory with experiment, is that the RRF factors obtained from the final water injections are reasonably close to the experimentally recorded values. A comparison between experimental and simulated RRF factors is given in Table 5.

5.3 Differences between adsorbed and bulk polymer

As remarked previously, the molecular weight of the adsorbed polymer can in the model be very different from the molecular weight of the flowing polymer. Since polymer adsorption is modelled as irreversible, it is the polymer from the first period of injection that sticks to the wall. This means that the RRF factor in our model becomes a function of the initial flow rate. The difference in molecular weight between polymer in the bulk fluid and adsorbed polymer is illustrated in Fig. 4. In the figure, we plot steady-state M_w values versus distance along the core for one of the experiments.

Figure 4 reveals that the polymer in bulk solution is quickly degraded near the inlet of the first core plug,

Table 5 Langmuir adsorption parameters used in the simulations

System id	Rock type	Q_m^1	Q_m^2	Polymer	RRF_1 model	RRF_2 model	RRF_1	RRF_2
1	Berea	0.00044	0.00052	530	1.95	2.28	2	2
2	Berea	0.00034	0.00034	1030	2.28	2.24	2	2
3	Berea	0.00042	0.00045	1530	3.33	3.68	3.4	3.4
4	Berea	0.00058	0.00063	1530	6.26	6.39	6.3	6.3
5	Berea	0.00028	0.00028	2030	3.50	3.38	3.6	3.6
6	Bentheim	0.00027	0.00027	1530	1.99	2.00	2	2

In all cases a value of $b = 1000000$ was used, and the maximum adsorption capacities are denoted by Q_m^1 and Q_m^2 for core 1 and core 2, respectively (pore volume fractions). The last five columns show comparisons between simulated and experimental RRF values

with progressive degradation at increasing flow rates. Furthermore, the degradation continues well into the second core. In contrast, the adsorbed polymer retains a very high molecular weight throughout the whole system, since the adsorption happened at a lower rate when not much polymer was degraded.

5.4 Effects of molecular weight

In Fig. 5, we have compared model versus experimental RF values for 4 different polymer types, all with a hydrolysis degree of 30%, but with varying molecular weight.

We observe that the model is able to capture the main trends of the different experiments, although the result for the 530 polymer is not as good as the others. The resistance factors are slightly over- or underestimated, depending on the case, but overall the match is remarkably good when we take into account that the input parameters used in the shear thickening and shear degradation models were kept constant for all polymers (Table 2).

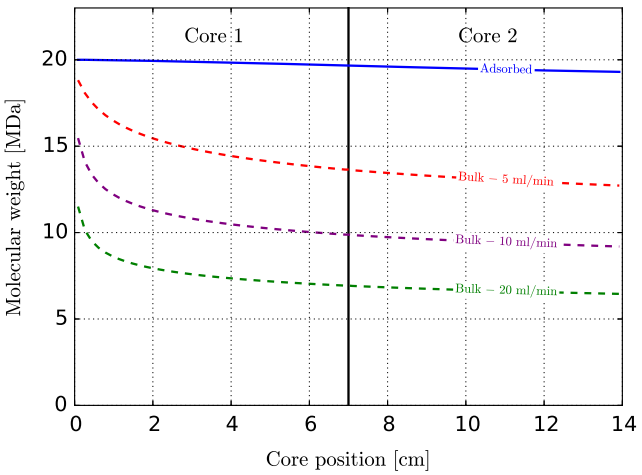

Fig. 4 Molecular weight in the water phase as a function of distance for the case of the 2030 HPAM polymer in the 823.6 mD and 800.4 mD dual core system. The spatial profile for the adsorbed polymer molecular weight is represented by the blue, solid line. The three dashed lines show spatial profiles of M_w at 3 different rates, all higher than the initial rate at which the adsorption occurred

If we replot the results from Fig. 5 using shear rate on the x-axis, we get the results in Fig. 6. Compared with Fig. 5, the profiles in Fig. 6 have a more even distribution for the onset of elongation, which is essentially a function of the polymer M_w and $[\eta]$, while the declining parts of the curves come closer together.

5.5 Effects of permeability

In order to look more closely at the effect of permeability, we have studied three of the experiments in more detail. In Fig. 7, we have plotted the simulated and experimental RF values for the 1530 HPAM polymer. We observe that the match is better for Core 1, and that the simulator overpredicts RF in the second core. About half of the decrease in RF, going from Core 1 to Core 2, is accounted for. One may also observe that the increasing part of RF is well matched for both cores in all three experiments, and that the horizontal shift of the curves due to different permeability is very well captured. Overall, considering experimental and model uncertainties, we find the result to be acceptable, as the trends are captured very well for all 3 permeabilities, and for both cores.

If we replot the results from Fig. 7 versus in situ shear rate, rather than applied flow rate, we get the results in Fig. 8. We observe that the curves fall more or less on top of each other, which is to be expected, because the onset of elongation is independent of permeability in the model. There is a difference in RF level at low shear rate, which can be rationalized by permeability dependent effects of a depletion layer, and by differences in RRF, see Table 5 and the further discussion below.

In Fig. 9, we plot predicted steady-state spatial profiles for the molecular weight in two of the simulations shown in Figs. 7 and 8. These plots confirm that more polymer degrades at lower permeability, and at higher applied flow rates.

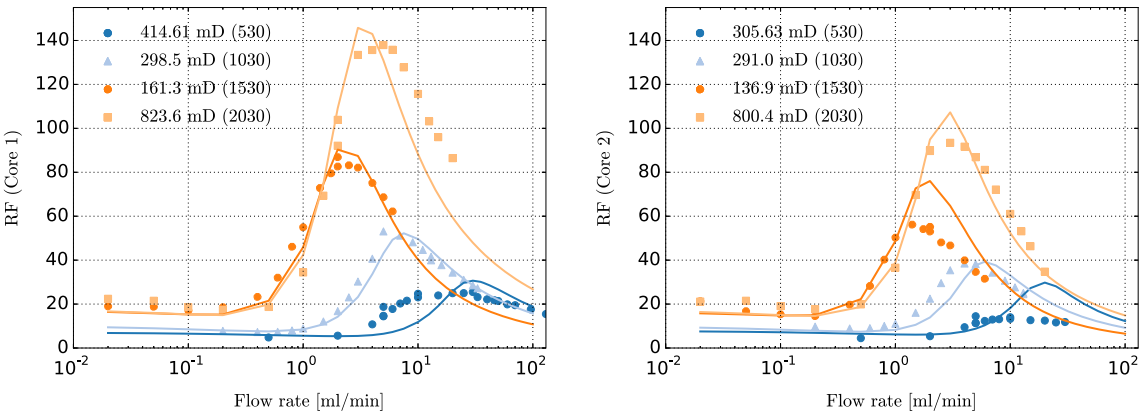

Fig. 5 Resistance factors plotted versus flow rate for 4 different polymer types, with M_w varied from 5 to 20 MDa. Dashed lines are from the simulator, whereas the points are derived from experimentally measured Δp and Q

5.6 Effects at low flow rates

Next, we show some examples of what can happen at low shear rates. In Fig. 10, we clearly see that the predicted RF factors are larger than the bulk viscosity, whereas the predicted apparent viscosity curves lie well below the bulk viscosity curves (Fig. 11). This is especially the case for the low permeable core. The reason for the large difference between RF and η for this core is the high $RRF = 6.3$. We observe that the bulk viscosity is closer to both RF and the apparent viscosity in the high permeability case, as expected due to the lower $RRF = 2$, and since the effect of a depletion layer become smaller at higher permeability. These plots illustrate nicely how the effects of permeability reduction and depletion layers can alter the in-situ rheology of the polymer (for an explanation of the depletion layer phenomenon, we refer to the discussion in Appendix A.1). However, we should point out that the experimental data at the lowest shear rates were of rather poor quality. Therefore, the clear differences between bulk and in situ rheology, shown in Figs. 10 and 11, may be smaller in reality.

5.7 Parameter discussion

All parameters and equations required for reproducing the simulations presented earlier are provided in the paper. The parameters can be separated into two groups, those representing measured properties directly (e.g., bulk polymer viscosity parameters and core permeability), and the other groups which are history matched to the core flood data.

All the history matched parameters were kept constant in simulations of the first series of core floods with HPAM in synthetic sea water. The history matched property was mainly the mobility reduction factor, RF, measured as a function of shear rate, and effluent viscosity indicating level of degradation. The observed RF is a result of three parts, the rate dependent polymer viscosity, a polymer depleted layer at the rock surface resulting in a reduced effective viscosity, and the permeability reduction factor, RRF. A value

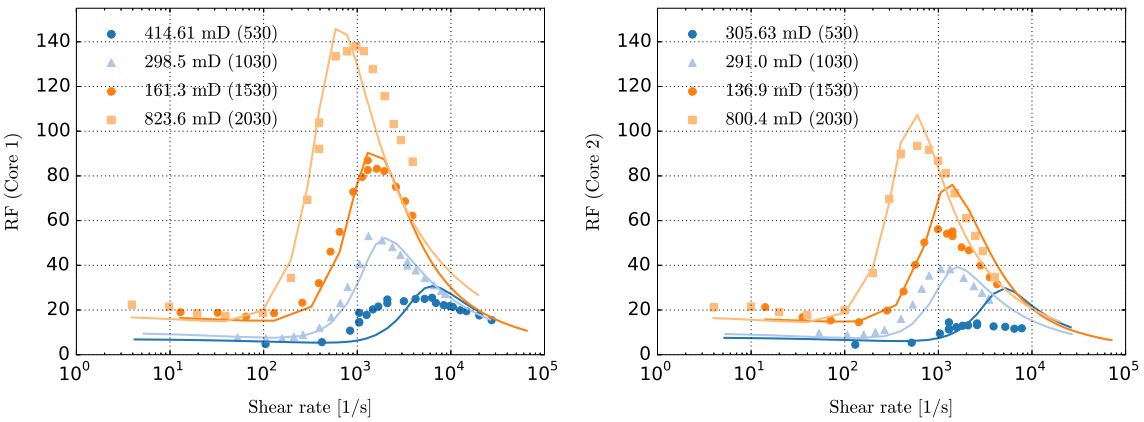

Fig. 6 Resistance factors plotted versus shear rate for 4 different polymer types. Dashed lines are from the simulator, whereas the points are derived from experimentally measured Δp and Q

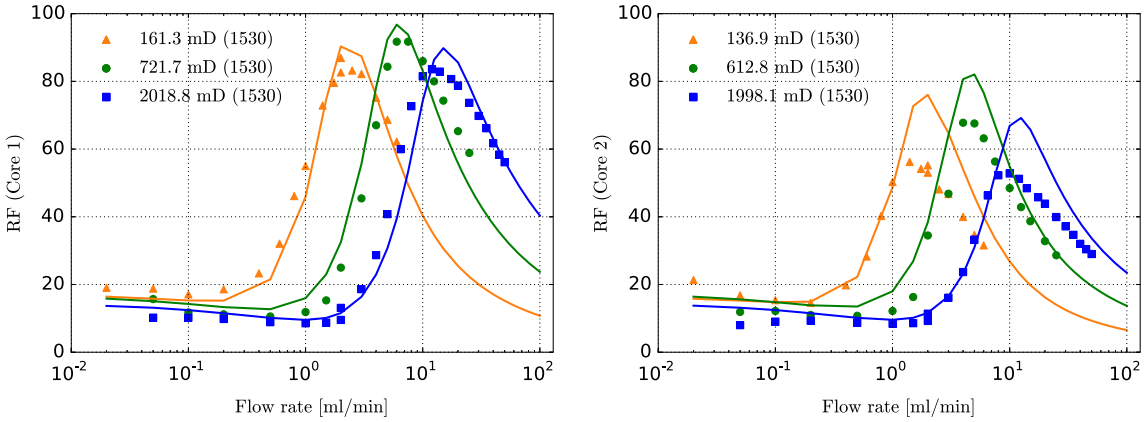

Fig. 7 Resistance factors for experiments performed with the 1530 HPAM polymer in 3 different serial core systems. The permeability varied from 137 mD to 2019 mD

for RRF is obtained at the end of the experiment, and the in situ polymer viscosity is computed from an apparent in situ shear rate.

The relative contributions from RRF and the depletion layer effect during polymer flooding are unknown and must be assumed. The polymer viscosity is based on measurements, however there are uncertainties in the tuning parameter used for in-situ apparent shear rate. Due to this, there will be a non-uniqueness in the parameters related to depletion layer and RRF that mainly affects the solution at lower shear rates. At higher shear rates, the depletion layer effect becomes small, and the relative contribution from elongational viscosity and RRF must be assumed. The effect of changing, e.g., the in-situ shear rate parameter from 2.0 to 1.0 would essentially change the critical Deborah number from 0.5 to 1.0 and result in a slight change in the degradation constant. The shear thickening and degradation would be matched as before, while the effect on the low shear end would be more uncertain.

6 Model test on a high viscosity dataset

The most novel parts of the model, those that deal with shear thickening and mechanical shear degradation, are very much based on experiments conducted with the same salinity (synthetic sea water) and the same polymer concentration (1500 ppm). As a final test, we apply the polymer model on a series of core flood experiments from Howe et al. [28], conducted in Bentheimer cores at very different salt and polymer concentrations. This test includes five core experiments performed with different HPAM polymers with M_w ranging from 3.6 to approximately 30 MDa, in low salinity brine (0.074 M) and viscosity at zero shear rate around 2 Pa s. That is, the effective salinity is roughly one order of magnitude lower than in the previous cases and, because of lower salinity and higher polymer concentrations, the viscosity is two orders of magnitude higher.

The bulk viscosity for the five polymers was matched with a single set of parameters given in Tables 1 and 6.

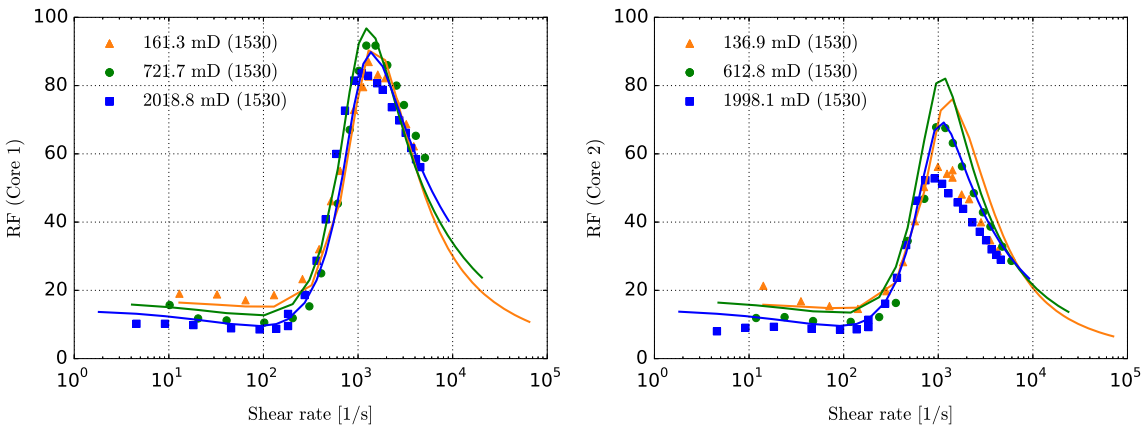

Fig. 8 Resistance factors plotted versus shear rate for experiments performed with the 1530 HPAM polymer in 3 different serial core systems. Dashed lines are from the simulator, whereas the points are derived from experimentally measured Δp and Q

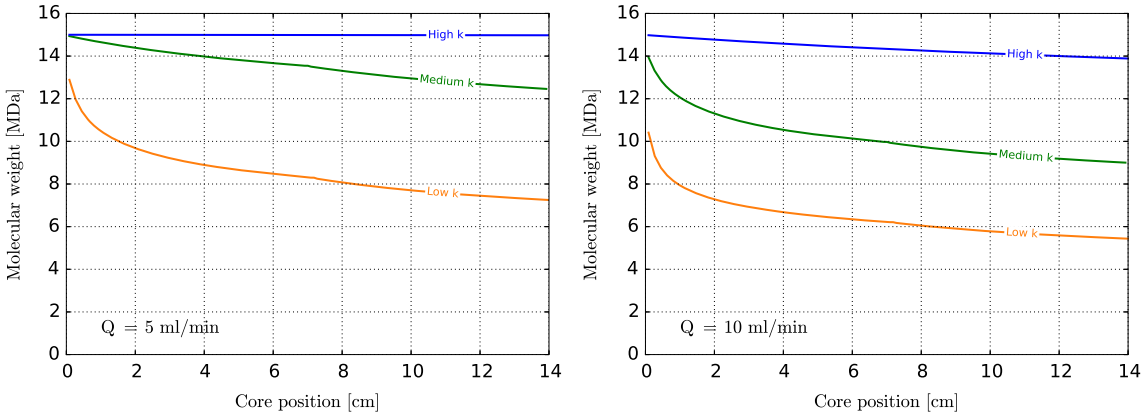

Fig. 9 Molecular weight in the water phase as a function of distance for the case of the 1530 HPAM polymer in cores with different permeability, i.e., for two of the cases shown in Figs. 7 and 8. The figures show the molecular weight inside the core at applied flow rates of, respectively, $Q = 5.0$ and 10.0 ml min^{-1}

The effective salinity model was activated, and C_s was computed as the sum of the brine strength (assumed to be 0.074 NaCl), and the polymer charge. A list of relevant computed properties is given in Table 6 (C_s, $[\eta]$, η_0, λ_1), in addition to polymer concentrations used, and the expressions for computing the salinity dependent values.

The matched shear thinning curves are plotted in Fig. 12. Points with increasing viscosity at the high shear rate end due to instabilities are removed. The results demonstrate the capability of the model, Eq. 21, to capture the onset of shear thinning over a large range in polymer concentration, intrinsic viscosity and molecular weight.

The core flood results with the five polymers are shown in Fig. 13. The core is a 3100 mD Bentheimer core with length 5 cm and diameter 3.8 cm. The original reported shear rate is corrected for the difference in expression used for in-situ shear rate with a factor around 3. No information was given about residual resistance factor RRF, so a reasonable salinity dependent adsorption was used to generate these values. The adsorption capacity, as well as the resulting RRF for each polymer, is given in Table 6.

If we ignore the degradation part of the model, we can compute resistance factors directly without any iteration. The lines in Fig. 13 represent such analytical calculations. From the figure, we see that the model matches the onset of shear thickening for all the polymers using the same critical Deborah number as in the previous cases ($N^{\star}_{De} = 0.5$). Two differences from the previous cases with seawater are that the transition between shear thinning and shear thickening is less sharp, and that the shear thickening increases more slowly. The transition parameter x_2 is reduced from 3 to 1.3 and the slope exponent m is reduced from 1.5 to 0.8, Eq. 23. This is a salinity effect also reported in, e.g., [7].

Another difference from the previous cases is the high viscosity contrast, which makes the computed result very sensitive to the depletion layer model at lower shear rates. In the simulations with much lower viscosity, the depletion layer thickness was assumed constant, and to only contain

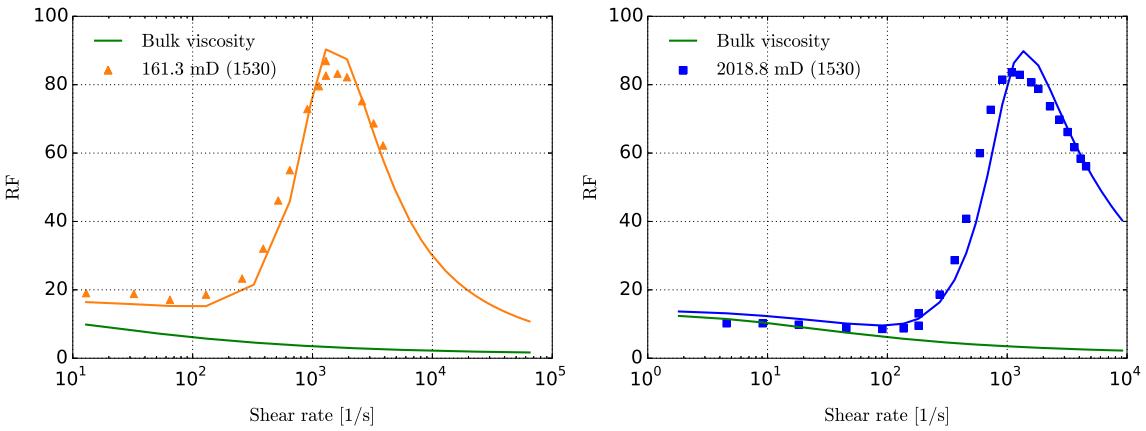

Fig. 10 Resistance factors versus shear rate for experiments performed with the 1530 HPAM polymer in high and low permeability cores. The green solid lines represents the predicted bulk viscosity of nondegraded polymer at the same shear rates

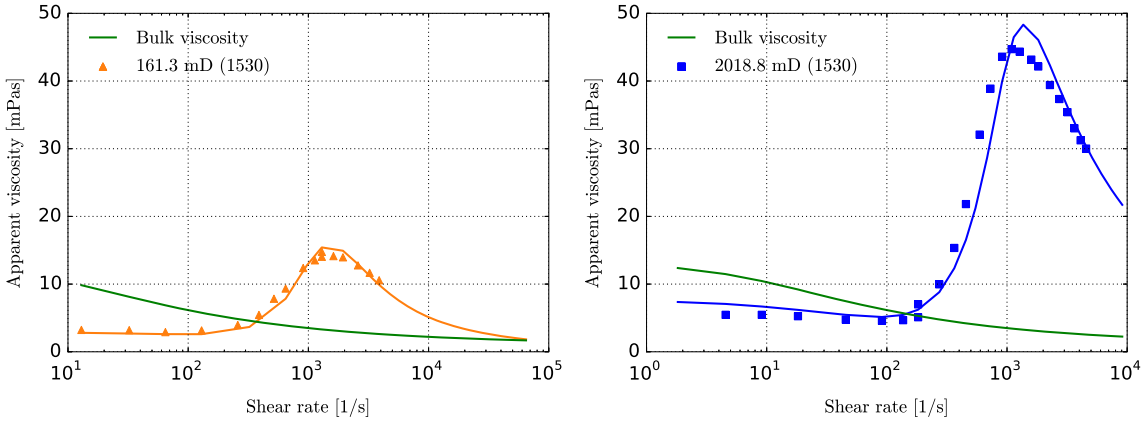

Fig. 11 Polymer apparent viscosity, η, versus shear rate for experiments performed with the 1530 HPAM polymer in high and low permeability cores. The green solid lines represents the predicted bulk viscosity of nondegraded polymer at the same shear rates

water. To capture the experimental flow resistance at lower shear rates, we set the polymer concentration in the depletion layer equal to 40% of that in the bulk solution ($c_{pd}/c_p^\star = 0.4$), and we required the depletion layer thickness to decrease with increasing polymer concentration by $\delta = R_h \cdot (c_p/0.001)^{-0.75}$ when $c_p > 0.001$ [45]. This model for the depletion layer captures a significant part of the shear thinning regime, but where the experimental curves level off the computed curves continue to increase with decreasing shear rate. This might indicate that there is a shear rate dependency involved as well, but as pointed out, other unknowns like adsorption and RRF may also play a role here.

The analytical solutions for two of the polymers are compared with simulations in Fig. 14. The simulations were run with the same model parameters as before, but now the effect of degradation is also included. The overlap between the analytical and simulated curves verifies the implementation of the model into the simulator. The simulated degradation towards high shear rate is not seen in the experiments. Experimental indication of an onset of degradation can only be seen for polymer 3630S as a levelling off in the resistance factor curve at high shear rate. This onset of degradation occurs at significantly higher shear rate than in the simulation, see Fig. 14. The simulations are run with the same degradation model parameters as used with polymer in seawater, and the overprediction clearly indicates that also degradation, at a given shear stress $\tau = \eta \cdot \dot{\gamma}$, is slowed down at lower salinity.

The simulations of the two experimental series show that the model handles the effect of molecular weight, permeability and porosity, as well as polymer concentration and salinity in the lower shear rate regime. The implemented polymer salinity model basically computes an effective salinity from the ionic composition of the brine and uses that effective salinity to correct the intrinsic viscosity. The effect of salinity is captured through the functional relationships of η_{sp0}, λ_1 and n on intrinsic viscosity (see Eqs. 4, 11 and 21).

The two data sets examined indicate that the onset of shear thickening, represented by λ_2 in Eq. 30, is captured through its salinity effect on $[\eta]$, while the reduced slope of the shear thickening and slower degradation at low salinity is not captured with the present model. Shear thickening behavior and mechanical degradation of the polymer can be

Table 6 Properties used to interpret experiments by Howe et al. [28]: effective salinity C_s, estimated RRF, polymer adsorption capacity Q_m (pore volume fraction), reference intrinsic viscosity used in salinity model $[\eta]_{ref} = 0.00139 \cdot M_w^{1.02}$, and intrinsic viscosity $[\eta] = [\eta]_{ref} \cdot C_s^{-0.4}$

Polymer	M_w	c_p	C_s	$[\eta]_{ref}$	$[\eta]$	RRF	Q_m	n	η_0	λ_1	ϕ	λ_2
6040S	31	0.0012	0.079	6091	16821	2.15	4.7E-5	0.557	1590	63.0	0.23	0.07691
3630S	18	0.00225	0.083	3498	9454	1.52	5.0E-5	0.564	1858	22.8	0.23	0.02517
3430S	11	0.00422	0.092	2117	5509	1.29	5.5E-5	0.575	2419	9.68	0.23	0.00901
3230S	6	0.00728	0.104	1659	2816	1.16	6.3E-5	0.559	1689	2.14	0.23	0.00253
3130S	3.6	0.0146	0.135	678	1508	1.11	8.1E-5	0.568	2118	0.80	0.23	0.00083

Shear thinning exponents, zero shear viscosities, and polymer relaxation times for the bulk solutions are displayed, based on input parameters from Table 1. In addition, values of λ_2 calculated for $\phi = 0.23$ are included. The HPAM hydrolysis degree was reported to be 40% for the 6040S polymer, and 30% for the rest. The dimensional quantities listed in the table have the following units: $[M_w]$ = MDa, $[C_s] = M$, $[\eta]_{ref} = [\eta] =$ ml g^{-1}, $[\eta_0]$ = mPas, $[\lambda_1] = [\lambda_2]$ = s

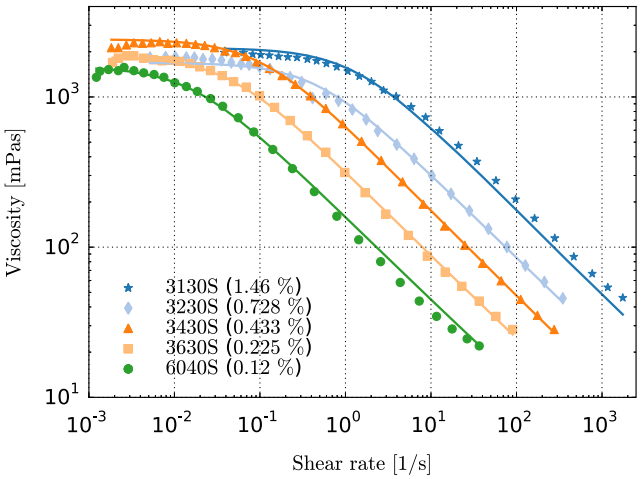

Fig. 12 Shear thinning bulk viscosity for polymers and concentrations given in Table 6

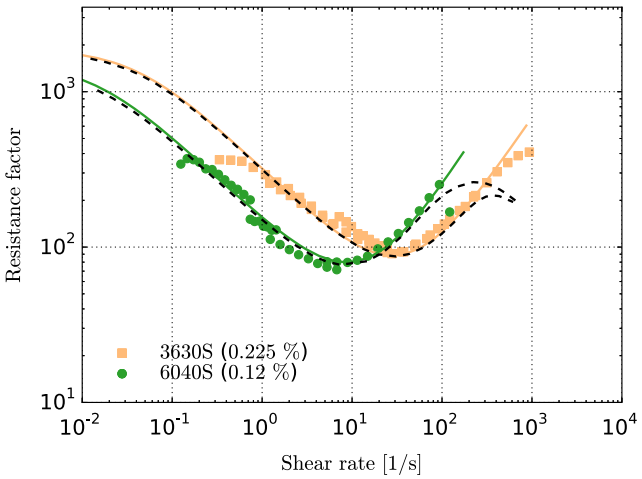

Fig. 14 Comparison of analytical solutions without degradation (solid lines) with simulations including degradation (dashed lines), for two polymers. The experimental data (points) are from Howe et al. [28]

represented by a single set of model parameters for a wide range of experiments if salinity is kept constant. If salinity is changed, then a separate set of model parameters must be used.

To include salinity effects into the shear thickening and shear degradation models, more experimental data with the same polymer at different salinities is needed. Some effects of salinity that may be important can be mentioned. When salinity is reduced, the relaxed size of the HPAM molecule will increase due to reduced electrostatic screening of charged polymer sites. The reduced difference in size between relaxed and stretched state might explain the reduced shear thickening slope and will probably also influence the degradation. Also, distribution of polymer in the shear plane close to mineral surfaces may be affected by, e.g., increased repulsive forces at low salinity. An effect of the latter is a reduction in adsorption.

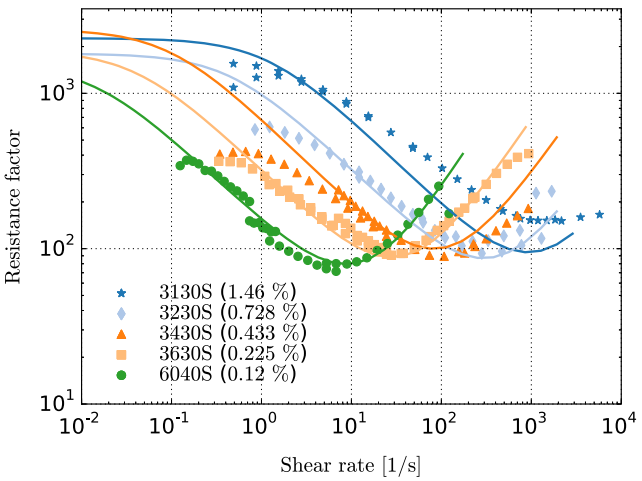

Fig. 13 Resistance factor versus flow rate for Bentheimer core experiments. The solid lines represent the model, whereas the experimental data (points) are adapted from Howe et al. [28]

7 Summary and conclusions

We have introduced a new model for simulating transport of polymer in a porous medium. A main focus has been to describe the flow properties of the polymeric fluids so that a correct relationship between flow rate and pressure drop across the core can be predicted. The model was primarily developed and tested in order to match shear thickening and degradation flow regimes inferred from single phase core-flooding experiments. A key aspect has been to relate the rheological parameters to conditions (temperature), properties of the porous media like permeability and porosity, and to fluid and polymer properties. To this end, we have in this work investigated the following factors:

- Effects of polymer concentration, c_p
- Effects of varying polymer molecular weight, M_w
- Effects of varying rock permeability k.

Possible effects of these variables have been included into the models controlling rheological properties, in particular the scaling groups controlling the onset of shear thinning and the onset of shear thickening, and the degradation model. The model has been applied on two series of core floods conducted with HPAM, the first with synthetic sea water and polymer viscosity up to 20 mPas, and the second test in a low salinity brine (0.074 M) with viscosities around 2 Pa s. The first series covers approximately one order of magnitude variation in both M_w and permeability. The second test has a similar variation in M_w and polymer concentration. The two series were matched with two separate input sets due to the difference in salinity.

Several salinity effects are included in the polymer model; however, a more thorough investigation is needed to obtain more precise information on the effect on shear

thickening and degradation parameters. Similarly, the proposed model includes several expressions to account for variations in temperature. The main effect of temperature is included via the solvent viscosity, but we expect that additional effects of temperature on the intrinsic viscosity might be needed. This is also something that needs to be explored in future work.

Acknowledgements The authors acknowledge the Research Council of Norway and the industry partners; ConocoPhillips Skandinavia AS, Aker BP ASA, Eni Norge AS, Maersk Oil Norway AS, DONG Energy A/S, Denmark, Statoil Petroleum AS, ENGIE E&P NORGE AS, Lundin Norway AS, Halliburton AS, Schlumberger Norge AS, Wintershall Norge AS of The National IOR Centre of Norway for support.

The authors would also like to thank two anonymous reviewers for their valuable feedback that helped us improve the quality of the paper.

Appendix

A.1 Excluded volume effects

A common observation in polymer flooding experiments is that the polymer travels at a higher flow rate than its solvent (water). This has been attributed to the large molecular size of the polymer molecules: If a rock contains a significant amount of small pores, not all of them will be available for polymer flow [15]. Furthermore, it has been observed that at low shear rates, effective viscosities estimated from core floods may be lower than corresponding bulk viscosity values [7, 8, 12, 45]. This behavior indicates a parallel flow of water depleted in polymer beside a flow of polymer rich solution. The flow of water may take place inside the micropores and/or in a polymer depleted layer at the pore surface. The idea here is that due to entropic considerations, large polymer molecules will be sterically excluded from layers of fluid close to the rock surface, preferring instead to flow near the centre of the pores.

In our model, we consider both types of inaccessible pore volume, i.e., we calculate

$$IPV = IPV_0 + IPV_d \cdot (1 - IPV_0)\,, \tag{44}$$

where IPV_0 denotes the fraction of pores that are totally inaccessible to the polymer ("micropores"), and IPV_d denotes the volume fraction of the depletion layer in the pores accessible for polymer. We assume negligible flow of water in the micropores, so the handling of IPV_0 is straightforward. The handling of IPV_d is more involved, and we only sketch the method here.

The flow in a capillary tube, representing a fraction $1 - IPV_0$ of the total volume, is divided into a polymer depleted phase and a polymer rich phase, with fractional flows of f_{dw} and f_p respectively. The depletion layer is represented by a layer at the tube surface with thickness δ. The fractional flows are obtained by integrating the Hagen-Poiseuille equation over the capillary tube, using constant viscosity in each of the two portions of the tube. Next, these results are combined with a single fluid solution for the capillary tube, after which the apparent polymer viscosity in the tube, η_{pa}, is obtained by requiring the same pressure gradient along the tube for the two cases.

Let $M_v = \eta_p/\eta_{dw}$ be the viscosity ratio between the two phases, where η_p is the viscosity in the polymer rich phase, and η_{dw} is the depletion layer viscosity. One can then show that

$$\eta_{pa} = \frac{\eta_p}{M_v - (M_v - 1)E_{PVd}^2}\,, \tag{45}$$

where

$$E_{PVd} = 1 - IPV_d = ((R - \delta)/R)^2 = (1 - \delta/R)^2\,, \tag{46}$$

with R being the tube radius. The apparent viscosity correction is applied after shear thinning but before including elongational effects, meaning that η_{sh} in Eq. 1 is used for calculating η_{pa} when the depletion model is activated. The thickness of the depletion layer is assumed to be in the range of the hydrodynamic radius R_h, but may decrease with increasing concentration above some critical concentration, c_{pd0} [45]. It is computed by

$$\delta = \begin{cases} f_{dpl} \cdot R_h & \text{if } c_p \le c_{pd0} \\ f_{dpl} \cdot R_h \cdot (c_p/c_{pd0})^{\alpha_{dp}} & \text{if } c_p > c_{pd0}\,, \end{cases} \tag{47}$$

where f_{dpl} and α_{dp} are tuning parameters. For all simulations presented in this paper, $f_{dpl} = 1$. We also need to handle the polymer concentration. The injected concentration is split into a polymer rich phase with concentration c_{pp}, and a water rich depleted layer at the pore surface where the polymer concentration is lower, c_{pd}. The average concentration in the rock is c_p, and $c_p^\star$ denotes the concentration after excluding the constant part of the inaccessible pore volume, but before incorporating the depletion layer effect. The relations between the different concentrations are given by

$$c_p^\star = \frac{c_p}{E_{PV0}} = c_{pp} \cdot E_{PVd}^\star\,. \tag{48}$$

where $E_{PVd}^\star = E_{PVd} - (1 - E_{PVd}) \cdot (c_{pd}/c_{pp})$, and where the last term is the relative polymer concentration in the depletion layer. The latter quantity is used to compute the depletion layer viscosity, η_{dw}, that enters the definition of M_v.

The polymer concentration c_{pp} will be higher than the injected concentration when the depletion layer model is activated. Moreover, the polymer rich phase will travel at a higher velocity than the polymer depleted phase close to

the surface. To capture this, we define an effective polymer concentration, c_{pef}, to be used in the transport equation for polymer. Mass balance considerations require the effective concentration to be equal to the injected concentration, c_p^{inj}, at steady state. Applying the mass balance, and combining with Eq. 48 and expressions for f_{dw} and f_p (not shown here), we obtain the following expression for the effective polymer concentration:

$$c_{pef} = c_p \cdot \frac{1}{E_{PV0}} \cdot \frac{2M_v(1 - E_{PVd^\star}) + E_{PVd^\star}}{M_v - (M_v - 1)E_{PVd^\star}^2} . \tag{49}$$

We remark that, for the low viscosity simulations presented in this paper, we assumed zero polymer concentration in the depleted layer, $c_{pd} = 0$. We also set the thickness δ of the depleted layer equal to the hydrodynamic radius of the polymer, $\delta = R_h$. On the other hand, for the simulations performed to match the dataset from Howe et al. [28], we used the more elaborate model reported herein. The exponent in Eq. 47 was then set to $\alpha_{dp} = -0.75$ [45], and $c_{pd}/c_{pp} = 0.4$.

A.2 Calculation of effective pore radius and in-situ shear rate

The shear rates experienced by the polymer molecules will vary drastically depending on the local conditions in the reservoir. In this paper, we have used the following correlation to calculate an average (effective) shear rate in porous media:

$$\dot{\gamma} = \dot{\gamma}_{pm} = \frac{4\alpha_c u}{\sqrt{8k\phi}} \cdot \sqrt{\frac{RRF}{1 - IPV_0}} . \tag{50}$$

Equation 50 is based on a model of the porous media as a bundle of capillary tubes, and the parameter α_c is a tuning parameter to account for variations in the pore geometry, whereas u is the Darcy velocity, and k is the permeability. We have explicitly included the fraction of pore volume that is totally inaccessible to the polymer, IPV_0, into the calculation of $\dot{\gamma}_{pm}$, as well as the permeability reduction factor, Eq. 37.

The effective pore radius for the flowing polymer, R_p, is calculated accordingly:

$$R_p = \sqrt{\frac{8kC}{\phi}} \cdot \frac{1}{\sqrt{RRF(1 - IPV_0)}} . \tag{51}$$

We should stress that we have no measurements of the IPV factor in our experiments. For convenience we have simply set it to a value of 0.1, i.e., we assume that 10% of the pores are too small for the polymer to enter. Small variations in α_c and IPV_0 do not greatly affect the results.

A.3 More on polymer adsorption and the permeability reduction model

By looking at the expression for the effective pore radius, Eq. 51, we see that the permeability scales with R_p^2/ϕ. Both of these factors are reduced by a factor $1 - A_{pt}$ when adsorbed polymer is introduced, and this justifies the use of Eq. 37. Moreover, it is not enough to simply take $A_{pt} \approx A_p$, because this does not consider the swelling (volumetric extension) of the adsorbed polymer inside the pores. Had we used $A_{pt} \approx A_p$, we would have to model unrealistically high levels of adsorption in order to match the experimentally determined RRF factors.

A more realistic model might also allow for desorption and re-adsorption of polymer molecules, in line with experimental data from the literature that suggests continuous exchange of lighter molecular weight species at the wall with higher molecular weight species from the solution [10]. However, in this work, we were only able to estimate the adsorption indirectly. We have therefore not considered such an extension to the model, as more data would be needed to properly test it.

We should also mention that in the model the adsorption capacity, Q_m, is scaled with $\sqrt{\phi/k}$, since a smaller effective pore size results in a larger available surface area for adsorption, see Eq. 51. A value of Q_m is specified at reference values k_{ref} and ϕ_{ref}, and Q_m at arbitrary k and ϕ becomes

$$Q_m = Q_m(k, \phi) = Q_m^{ref} \cdot \sqrt{\frac{k_{ref}}{k}} \cdot \sqrt{\frac{\phi}{\phi_{ref}}} . \tag{52}$$

The ability to vary Q_m is important for upscaling to the field, since there are large variations in permeability and porosity in the reservoir.

A.4 Effective salinity model

The effect of solution salinity is included in the simulator by making $[\eta]$ in Eq. 11 salinity dependent. For the present purposes, we calculate $[\eta]$ as a power-law of an effective salinity parameter, C_s:

$$[\eta] = [\eta]_{ref} \cdot C_s^{\alpha_s} . \tag{53}$$

The parameter $[\eta]_{ref}$ is a reference intrinsic viscosity, calculated from the polymer molecular weight, and α_s is a fitting parameter which can be obtained as the slope of the intrinsic viscosity versus effective salinity on a log-log plot. The effective salinity is calculated as a weighted sum of the ionic concentrations in the solution:

$$C_s = \sum_i C_i \beta_i . \tag{54}$$

Here, β_i is a constant that varies according to the valence of ion i, and C_i is the molar concentration. NaCl is used as

a reference salt with $\beta_{Na} = \beta_{Cl} = 0.5$ so that C_s for a pure NaCl electrolyte becomes equal to the molar concentration. Other ions have β_i expressing their relative strength to either Na^+ or Cl^-. A common method is to set C_s equal to the ionic strength,

$$I = \frac{1}{2} \sum_i C_i z_i^2 \,, \tag{55}$$

which would put more weight on divalent ions and in our notation have $\beta_{Ca} = 2$. Investigations on interaction forces between ions and charged surfaces like clay or charged molecules like surfactant have shown that not only the valence, but also the hydrated sizes of the ions are important [48]. The ionic strength expression may severely underestimate the effect of divalent ions, and Stavland et al. [65] used a "modified ionic strength" where the power of the valence term was allowed to be higher than 2 for divalent ions. The presented data indicated an order of magnitude higher effect from Ca^{2+} on the polymer viscosity, i.e., $\beta_{Ca} \approx 20$.

A.5 Temperature effects

In the current model, it is assumed that the main temperature dependence of the effective viscosity is captured by the viscosity of the solvent, which is computed according to an Arrhenius equation. Additionally, we have seen that both relaxation time constants, λ_1 and λ_2, are inverse functions of temperature, since they are related to diffusion. However, as we have only considered experiments performed at room temperature (20 °C), more experimental data is needed in order to test this part of the model.

References

1. Al Hashmi, A., Al Maamari, R., Al Shabibi, I., Mansoor, A., Zaitoun, A., Al Sharji, H.: Rheology and mechanical degradation of high-molecular-weight partially hydrolyzed polyacrylamide during flow through capillaries. J. Pet. Sci. Eng. **105**, 100–106 (2013)
2. Bird, R.B., Armstrong, R.C., Hassager, O.: Dynamics of Polymeric Liquids, Fluid Mechanics, 2nd edn., vol. 1. Wiley, New York (1987)
3. Bird, R.B., Curtiss, C.F., Armstrong, R.C., Hassager, O.: Dynamics of Polymer Liquids, Kinetic, Theory, 2nd edn., vol. 2, p. 2. Wiley, New York (1987)
4. Bird, R.B., Stewart, W.E., Lightfoot, E.N.: Transport Phenomena. Wiley, New York (2002)
5. Brakstad, K., Rosenkilde, C.: Modelling viscosity and mechanical degradation of polyacrylamide solutions in porous media. In: SPE Improved Oil Recovery Conference. Society of Petroleum Engineers (2016)
6. Buchholz, B.A., Zahn, J.M., Kenward, M., Slater, G.W., Barron, A.E.: Flow-induced chain scission as a physical route to narrowly distributed, high molar mass polymers. Polymer **45**(4), 1223–1234 (2004)
7. Chauveteau, G.: Molecular interpretation of several different properties of flow of coiled polymer solutions through porous media in oil recovery conditions. In: SPE Annual Technical Conference and Exhibition, SPE-10060-MS. Society of Petroleum Engineers (1981)
8. Chauveteau, G.: Fundamental criteria in polymer flow through porous media and their relative importance in the performance differences of mobility control buffers. In: Glass, J. (ed.) Water-Soluble Polymers, vol. 213, pp. 227–268. Advances in Chemistry Series of the American Chemical Society (1986)
9. Chauveteau, G., Moan, M.: The onset of dilatant behaviour in non-inertial flow of dilute polymer solutions through channels with varying cross-sections. J. Phys. Lett. **42**(10), 201–204 (1981)
10. Chauveteau, G., Lecourtier, J.: Propagation of polymer slugs through adsorbent porous media. In: Water-Soluble Polymers for Petroleum Recovery, pp. 53–68. Springer (1988)
11. Chauveteau, G., Moan, M., Magueur, A.: Thickening behaviour of dilute polymer solutions in non-inertial elongational flows. J. Non-Newtonian Fluid Mech. **16**(3), 315–327 (1984)
12. Chauveteau, G., Tirrell, M., Omari, A.: Concentration dependence of the effective viscosity of polymer solutions in small pores with repulsive or attractive walls. J. Colloid Interface Sci. **100**(1), 41–54 (1984)
13. Chauveteau, G., Denys, K., Zaitoun, A.: New insight on polymer adsorption under high flow rates. In: SPE/DOE Improved Oil Recovery Symposium. Society of Petroleum Engineers (2002)
14. Clay, J., Koelling, K.: Molecular degradation of concentrated polystyrene solutions in a fast transient extensional flow. Polym. Eng. Sci. **37**(5), 789–800 (1997)
15. Dawson, R., Lantz, R.B.: Inaccessible pore volume in polymer flooding. Soc. Pet. Eng. J. **12**(05), 448–452 (1972)
16. De Gennes, P.: Coil-stretch transition of dilute flexible polymers under ultrahigh velocity gradients. J. Chem. Phys. **60**(12), 5030–5042 (1974)
17. Delshad, M., Kim, D.H., Magbagbeola, O.A., Huh, C., Pope, G.A., Tarahhom, F.: Mechanistic interpretation and utilization of viscoelastic behavior of polymer solutions for improved polymer-flood efficiency. In: SPE Symposium on Improved Oil Recovery. Society of Petroleum Engineers (2008)
18. Dill, K., Bromberg, S.: Molecular driving forces: Statistical thermodynamics in biology, chemistry, physics, and nanoscience. Garland Science (2010)
19. Dupas, A., Hénaut, I., Argillier, J.F., Aubry, T.: Mechanical degradation onset of polyethylene oxide used as a hydrosoluble model polymer for enhanced oil recovery. Oil Gas Sci. Technol.–Revue d'IFP Energies nouvelles **67**(6), 931–940 (2012)
20. ECLIPSE, Industry-Reference Reservoir Simulator Technical Description, Schlumberger, 2016 (Version 2016.1)
21. Flory, P.J.: Principles of Polymer Chemistry. Cornell University Press (1953)
22. Ford, J.: Improved algorithms of Illinois-type for the numerical solution of nonlinear equations. Tech. Rep. CSM-257 University of Essex (1995)
23. Haas, R., Durst, F.: Viscoelastic flow of dilute polymer solutions in regularly packed beds. In: Progress and Trends in Rheology, pp. 212–217. Springer (1982)
24. Hatzignatiou, D.G., Norris, U.L., Stavland, A.: Core-scale simulation of polymer flow through porous media. J. Pet. Sci. Eng. **108**, 137–150 (2013)
25. Haward, S.: Microfluidic extensional rheometry using stagnation point flow. Biomicrofluidics **10**(4), 043,401 (2016)
26. Hiemenz, P.C., Lodge, T.P.: Polymer Chemistry, 2nd edn. CRC Press (2007)
27. Hirasaki, G., Pope, G.: Analysis of factors influencing mobility and adsorption in the flow of polymer solution through porous media. Soc. Pet. Eng. J. **14**(04), 337–346 (1974)

28. Howe, A.M., Clarke, A., Giernalczyk, D.: Flow of concentrated viscoelastic polymer solutions in porous media: effect of M_w and concentration on elastic turbulence onset in various geometries. Soft Matter **11**(32), 6419–6431 (2015)
29. Hu, X., Boukany, P.E., Hemminger, O.L., Lee, L.J.: The use of microfluidics in rheology. Macromolec. Mater. Eng. **296**(3-4), 308–320 (2011)
30. Idahosa, P., Oluyemi, G., Oyeneyin, M., Prabhu, R.: Rate-dependent polymer adsorption in porous media. J. Pet. Sci. Eng. **143**, 65–71 (2016)
31. Islam, M.T., Vanapalli, S.A., Solomon, M.J.: Inertial effects on polymer chain scission in planar elongational cross-slot flow. Macromolecules **37**(3), 1023–1030 (2004)
32. Jouenne, S., Anfray, J., Levitt, D., Souilem, I., Marchal, P., Lemaitre, C., Choplin, L., Nesvik, J., Waldman, T.: Degradation (or lack thereof) and drag reduction of HPAM solutions during transport in turbulent flow in pipelines. Oil Gas Facilit. **4**(01), 80–92 (2015)
33. Kawale, D., Marques, E., Zitha, P.L., Kreutzer, M.T., Rossen, W.R., Boukany, P.E.: Elastic instabilities during the flow of hydrolyzed polyacrylamide solution in porous media: Effect of pore-shape and salt. Soft Matter (2017)
34. Keller, A., Odell, J.: The extensibility of macromolecules in solution; a new focus for macromolecular science. Colloid. Polym. Sci. **263**(3), 181–201 (1985)
35. Lake, L.W.: Enhanced Oil Recovery. Prentice Hall Inc., Old Tappan (1989)
36. Lange, E., Huh, C.: A polymer thermal decomposition model and its application in chemical EOR process simulation. In: SPE/DOE Improved Oil Recovery Symposium. Society of Petroleum Engineers (1994)
37. Lee, A.: A Polymer Hydrolysis Model and its Application in Chemical EOR Process Simulation. http://hdl.handle.net/2152/ETD-UT-2010-12-2579. Master of Science report, University of Texas, Austin (2010)
38. Machado, A., Bodiguel, H., Beaumont, J., Clisson, G., Colin, A.: Extra dissipation and flow uniformization due to elastic instabilities of shear-thinning polymer solutions in model porous media. Biomicrofluidics **10**(4), 043,507 (2016)
39. Maerker, J.: Shear degradation of partially hydrolyzed polyacrylamide solutions. Soc. Pet. Eng. J. **15**(04), 311–322 (1975)
40. Masuda, Y., Tang, K.C., Miyazawa, M., Tanaka, S.: 1D simulation of polymer flooding including the viscoelastic effect of polymer solution. SPE Reservoir Eng. **7**(02), 247–252 (1992)
41. Morel, D., Zaugg, E., Jouenne, S., Danquigny, J., Cordelier, P.: Dalia/Camelia polymer injection in deep offshore field Angola learnings and in situ polymer sampling results. In: SPE Asia Pacific Enhanced Oil Recovery Conference. Society of Petroleum Engineers (2015)
42. Nguyen, T., Kausch, H.H.: Influence of nozzle geometry on polystyrene degradation in convergent flow. Colloid. Polym. Sci. **269**(11), 1099–1110 (1991)
43. Nguyen, T.Q., Kausch, H.H.: Chain scission in transient extensional flow kinetics and molecular weight dependence. J. Non-Newtonian Fluid Mech. **30**(2-3), 125–140 (1988)
44. Odell, J., Keller, A., Rabin, Y.: Flow-induced scission of isolated macromolecules. J. Chem. Phys. **88**(6), 4022–4028 (1988)
45. Omari, A., Moan, M., Chauveteau, G.: Wall effects in the flow of flexible polymer solutions through small pores. Rheol. Acta **28**(6), 520–526 (1989)
46. OPM, The Open Porous media Initiative, http://opm-project.org/. Accessed 18 March 2017
47. Perkins, T.T., Smith, D.E., Chu, S.: Single polymer dynamics in an elongational flow. Science **276**(5321), 2016–2021 (1997)
48. Puerto, M.C., Reed, R.L.: Surfactant selection with the three-parameter diagram. SPE Reserv. Eng. **5**(02), 198–204 (1990)
49. Rajagopalan, R., Hiemenz, P.C.: Principles of Colloid and Surface Chemistry, 3rd edn. CRC Press (1997)
50. Rems, L., Kawale, D., Lee, L.J., Boukany, P.E.: Flow of DNA in micro/nanofluidics: From fundamentals to applications. Biomicrofluidics **10**(4), 043,403 (2016)
51. Seright, R.S.: The effects of mechanical degradation and viscoelastic behavior on injectivity of polyacrylamide solutions. Soc. Pet. Eng. J. **23**(03), 475–485 (1983)
52. Seright, R.S., Fan, T., Wavrik, K., Balaban, R.D.C.: New insights into polymer rheology in porous media. SPE J. **16**(01), 35–42 (2011)
53. Shaqfeh, E.S.: The dynamics of single-molecule DNA in flow. J. Non-Newtonian Fluid Mech. **130**(1), 1–28 (2005)
54. Sharma, A., Delshad, M., Huh, C., Pope, G.A.: A practical method to calculate polymer viscosity accurately in numerical reservoir simulators. In: SPE Annual Technical Conference and Exhibition. Society of Petroleum Engineers (2011)
55. Sheng, J.J., Leonhardt, B., Azri, N.: Status of polymer-flooding technology. J. Can. Pet. Technol. **54**(02), 116–126 (2015)
56. Simulators / Computer Resources, Center for Petroleum and Geosystems Engineering, The University of Texas at Austin, http://www.cpge.utexas.edu/?q=iap_rsjip_simulators/. Accessed 18 March 2017
57. Smith, D.E., Chu, S.: Response of flexible polymers to a sudden elongational flow. Science **281**(5381), 1335–1340 (1998)
58. Smith, D.E., Babcock, H.P., Chu, S.: Single-polymer dynamics in steady shear flow. Science **283**(5408), 1724–1727 (1999)
59. Sorbie, K., Roberts, L.: A model for calculating polymer injectivity including the effects of shear degradation. In: SPE Enhanced Oil Recovery Symposium. Society of Petroleum Engineers (1984)
60. Sorbie, K.S.: Polymer-improved Oil Recovery. Springer Science & Business Media (1991)
61. Southwick, J., Manke, C.: Molecular degradation, injectivity, and elastic properties of polymer solutions. SPE Reserv. Eng. **3**(04), 1–193 (1988)
62. Spillette, A., Hillestad, J., Stone, H.: A high-stability sequential solution approach to reservoir simulation. In: Fall Meeting of the Society of Petroleum Engineers of AIME. Society of Petroleum Engineers (1973)
63. STARS Resource Library, Computer Modelling Group Ltd., http://www.cmgl.ca/stars/resource-library/. Accessed 18 March 2017
64. Stavland, A., Jonsbroten, H., Lohne, A., Moen, A., Giske, N.: Polymer flooding–flow properties in porous media versus rheological parameters. In: Presented at the 72nd EAGE Conference and Exhibition incorporating SPE EUROPEC, SPE-131103-MS (2010)
65. Stavland, A., Jonsbråten, H., Strand, D.: When will polymer viscosity be a design criterion for EOR polymer flooding. In: IEA-EOR 34th Annual Symposium, pp. 8–11. Stavanger (2013)
66. Teixeira, R.E., Babcock, H.P., Shaqfeh, E.S., Chu, S.: Shear thinning and tumbling dynamics of single polymers in the flow-gradient plane. Macromolecules **38**(2), 581–592 (2005)
67. Thomas, A., Gaillard, N., Favero, C.: Some key features to consider when studying acrylamide-based polymers for chemical enhanced oil recovery. Oil Gas Sci Technol–Revue d'IFP Energies nouvelles **67**(6), 887–902 (2012)
68. Vanapalli, S.A., Islam, M.T., Solomon, M.J.: Scission-induced bounds on maximum polymer drag reduction in turbulent flow. Phys. Fluids **17**(9), 095,108 (2005)
69. Vanapalli, S.A., Ceccio, S.L., Solomon, M.J.: Universal scaling for polymer chain scission in turbulence. Proc. Nat. Acad. Sci. **103**(45), 16,660–16,665 (2006)
70. Watts, J.: A compositional formulation of the pressure and saturation equations. SPE Reserv. Eng. **1**(03), 243–252 (1986)
71. Yasuda, K., Armstrong, R., Cohen, R.: Shear flow properties of concentrated solutions of linear and star branched polystyrenes. Rheol. Acta **20**(2), 163–178 (1981)
72. Zhang, G., Seright, R.: Effect of concentration on HPAM retention in porous media. SPE J. **19**(03), 373–380 (2014)